Continuum contact model for friction between graphene sheets that accounts for surface anisotropy and curvature

Aningi Mokhalingam[1], Shakti S. Gupta[1], and Roger A. Sauer[2,3,4,*]
[1]*Department of Mechanical Engineering, Indian Institute of Technology Kanpur, Kanpur UP 208016 India*
[2]*Aachen Institute for Advanced Study in Computational Engineering Science (AICES), RWTH Aachen University, 52056 Aachen, Germany*
[3]*Faculty of Civil and Environmental Engineering, Gdańsk University of Technology, 80-233 Gdańsk, Poland*
[4]*Department of Mechanical Engineering, Indian Institute of Technology Guwahati, Assam 781039, India*

(Received 15 September 2023; revised 22 December 2023; accepted 3 January 2024; published 29 January 2024)

Understanding the interaction mechanics between graphene layers and coaxial carbon nanotubes (CNTs) is essential for modeling graphene and CNT-based nanoelectromechanical systems. This work proposes a new continuum contact model to study interlayer interactions between curved graphene sheets. The continuum model is calibrated and validated using molecular dynamics (MD) simulations. These are carried out employing the reactive empirical bond order (REBO)+Lennard-Jones (LJ) potential to model the interactions within a sheet, while the LJ, Kolmogorov-Crespi (KC), and Lebedeva potentials are used to model the interactions between sheets. The continuum contact model is formulated for separation distances greater than 0.29 nm, when sliding contact becomes nondissipative and can be described by a potential. In this regime, sheet deformations are sufficiently small and do not affect the sheet interactions substantially. This allows to treat the master contact surface as rigid, thus simplifying the contact formulation greatly. The model calibration is conducted systematically for a sequence of different stackings using existing and newly proposed ansatz functions. The calibrated continuum model is then implemented in a curvilinear finite-element (FE) shell formulation to investigate the pull-out and twisting interactions between coaxial CNTs. The resisting pull-out forces and torques depend strongly on the chirality of the considered CNTs. The absolute differences between FE and MD results are very small and can be attributed to model assumptions and loading conditions.

DOI: 10.1103/PhysRevB.109.035435

I. INTRODUCTION

Graphene is a two-dimensional (2D) material with tightly packed carbon atoms in a hexagonal lattice structure that can be isolated from bulk graphite through micromechanical exfoliation [1]. Experimental studies have shown that bi- and multilayer graphene have remarkable thermomechanical and tribological properties [2–4]. The strong in-plane covalent bonds and weak nonbonded forces between the layers offer tunability of properties through different stackings. In particular, interlayer twisting or stretching of bilayer graphene can result in superlubricity and superconductivity [5–8]. Due to these tunable properties, multilayered graphene has the potential to be used in various engineering applications [9–11].

The interaction mechanics of graphene layers has been studied using different techniques, viz., experiments [3,5,12], theory [2,13–18], and atomistic simulations [19–25]. For instance, Dienwiebel *et al.* [5] measured ultralow friction or superlubricity between graphene layers due to incommensurability obtained through the relative rotation between the graphene layers using a frictional force microscope. The superlubricity in twisted bilayer graphene and graphene heterojunctions is governed by Moiré patterns formed between the mismatched layers [14,26,27]. In another work, Dienwiebel *et al.* [12] reported anisotropic friction with an angular periodicity of 60°. Verhoeven *et al.* [2] investigated rigid graphene flake interactions over a graphene surface employing the modified Prandtl-Tomlinson model [28] and reported that the frictional forces depend on the flake size and relative rotation between the graphene flake and substrate. Further, they have approximated the interaction energy using only the first Fourier components with the wavelengths $\sqrt{3}a_{\mathrm{cc}}$, $1.5a_{\mathrm{cc}}$, and $3a_{\mathrm{cc}}$, where a_{cc} is the covalent C-C bond length. Using the Lennard-Jones (LJ) potential, Xu *et al.* [20] investigated the influence of the number of graphene layers on stick-slip friction and reported that these forces reduce with a decrease in the number of layers. Wang *et al.* [17] studied the size effect on the interlayer shear behavior in bilayer graphene, accounting for elastic deformation in the graphene sheets employing a nonlinear shear-lag model [29]. They reported that the maximum shear force depends on the length and width of the sheet. However, for a length beyond 20 nm, the shear force is constant due to nonuniform relative displacement between the sheets. Using first-principles calculations, Sun *et al.* [30] reported that bilayer graphene sliding friction reduces with increasing sheet contact pressure[1] and becomes zero at

---

[*] roger.sauer@pg.edu.pl; sauer@aices.rwth-aachen.de

[1] The common term *contact pressure* is used to denote the pressure between two graphene sheets even though they always remain at a nanoscale distance.

a critical point due to the transition of the potential energy surface from a corrugated to a flattened and to a counter-corrugated state. Using the finite-element method, Xue *et al.* [18] studied the dynamics of peeling and sliding graphene nanoribbons on a graphene substrate and reported that adhesive and shear interactions of graphene sheets influence the sliding behavior. Afsharirad *et al.* [25] studied the interlayer interactions between the walls of double-walled carbon nanotubes (DWCNT) using the LJ potential and reported that zigzag CNTs[2] show larger axial sliding resistance than other kinds of CNTs. Arroyo and Belytschko [31–33] formulated a continuum contact theory for curved monolayer lattices via the exponential Cauchy-Born rule and implemented it in the finite-element method to investigate the mechanics of CNTs.

The variation of the interaction energy with the relative displacement of two graphene sheets is dominated by their π-orbital overlap at lower separation distances [34]. The corrugation amplitude of the potential relief at these lower separation distances obtained from the LJ potential underestimates the interactions. This lead to the development of various new interaction potentials: the KC potential [34], a registry-dependent interlayer potential, the potential of Lebedeva *et al.* [35], a potential enriched with density-functional theory (DFT) data, the potential of Jiang and Park [36], a modification of the LJ potential by introducing Gaussian terms, the potential of Wen *et al.* [37], a modification of the KC potential by adding a dihedral-angle-dependent term to the repulsive part, and the potential of Leven and Maaravi *et al.* [38,39], a potential considering many-body dispersion effects. These potentials are successful in predicting the bulk properties of graphitic systems [40].

The general continuum description of anisotropic friction based on frame-invariant tensors goes back to the works of Zmitrowicz [41–43]—covering both centrosymmetric (forward/backward equivalent) and noncentrosymmetric (forward/backward different) anisotropic friction. Tensorial descriptions have become the basis for general nonlinear finite-element (FE) formulations for frictional contact [44,45]. The first nonlinear FE formulations for centrosymmetric anisotropic friction go back to the works of Park and Kwak [46] and Buczkowski and Kleiber [47]. Subsequently, these formulations have been extended to noncentrosymmetric friction [48], anisotropic sticking [49,50], boundary-element methods [51] and isogeometric analysis [52], and they have been used in the computational study of various applications, such as wear [53], contact homogenization [52,54], and droplet sliding [55]. Recent works have also proposed general coupling models for friction and adhesion for isotropic friction [56,57] and anisotropic friction [58].

Here we develop a new continuum contact model for simulating and studying the nondissipative anisotropic interaction of curved graphene bilayers. The continuum model is calibrated from near-zero Kelvin molecular dynamics (MD) simulations within the range of their validity. The MD simulations employ the reactive empirical bond order (REBO)+LJ potential to model the strong covalent interactions of carbon atoms within the sheets and employ various long-range interaction potentials to model the interactions between the two sheets. A nonlinear finite-element contact formulation is then implemented using the calibrated continuum contact model. The proposed model is validated from the pull-out and twisting of DWCNTs. In summary, the novelties of the current work are as follows:

(i) Formulation of a continuum contact model for curved commensurate graphene sheets.

(ii) Calibration of the model from MD data across a wide range of contact pressures.

(iii) Nonlinear finite-element implementation of the model.

(iv) Application of the model to the pull-out and twisting of CNTs from/within DWCNTs.

(v) Validation and verification of the model using MD data and analytical results.

The remainder of the paper is organized as follows: The atomic simulation procedure and their interatomic potentials are described in Sec II. The description of the continuum interaction model, contact kinematics, and tractions are given in Sec. III. The model calibration and behavior for flat bilayer graphene sliding are presented in Sec. IV. The finite-element formulation and the numerical results of CNT pull-out and twisting are then described in Secs. V and VI, respectively, followed by conclusions in Sec. VII.

II. MOLECULAR SIMULATIONS

In order to calibrate the proposed continuum model, molecular simulations of the interaction between two graphene sheets are used. The simulated sheets are approximately square with size 10.08 nm × 10.16 nm. The covalent and long-range bond interactions between the carbon atoms within graphene are modeled using the second generation REBO+LJ [59] potential, while the long-range bond interactions between the sheets are modeled using the LJ [60], KC [34], or Lebedeva [35] potentials (see Appendix A for details).

We relax the system before applying tangential sliding between the layers. The bilayer graphene system is brought to the minimum energy configuration using the Polak-Ribiere conjugate gradient method [61]. Subsequently, the system is thermally equilibrated at 0.1 K employing the Nosé-Hoover thermostat [62] with three Nosé-Hoover chains. Once the relaxed state is achieved, the lower layer is kept fixed by constraining all the degrees of freedom of the atoms. The top sheet is then pulled along the armchair or zigzag direction ($\boldsymbol{e}_a$ or $\boldsymbol{e}_z$ in Fig. 1) parallel to the bottom layer by providing a constant velocity of 0.01 Å/ps to all atoms lying on the four edges. While sliding, the lateral movement of the edge atoms of the top sheet is constrained. The resistance of the top sheet to sliding, i.e., the tangential traction, is determined from

$$\boldsymbol{t}_t = \sum_{I=1}^{N} \boldsymbol{F}_I / A, \tag{1}$$

where $\boldsymbol{F}_I$ is the tangential component of the van der Waals (vdW) force acting on atom I due to the bottom layer, A is

---

[2] Zigzag CNTs have zigzag circumference and armchair axis, while it is the opposite for armchair CNTs.

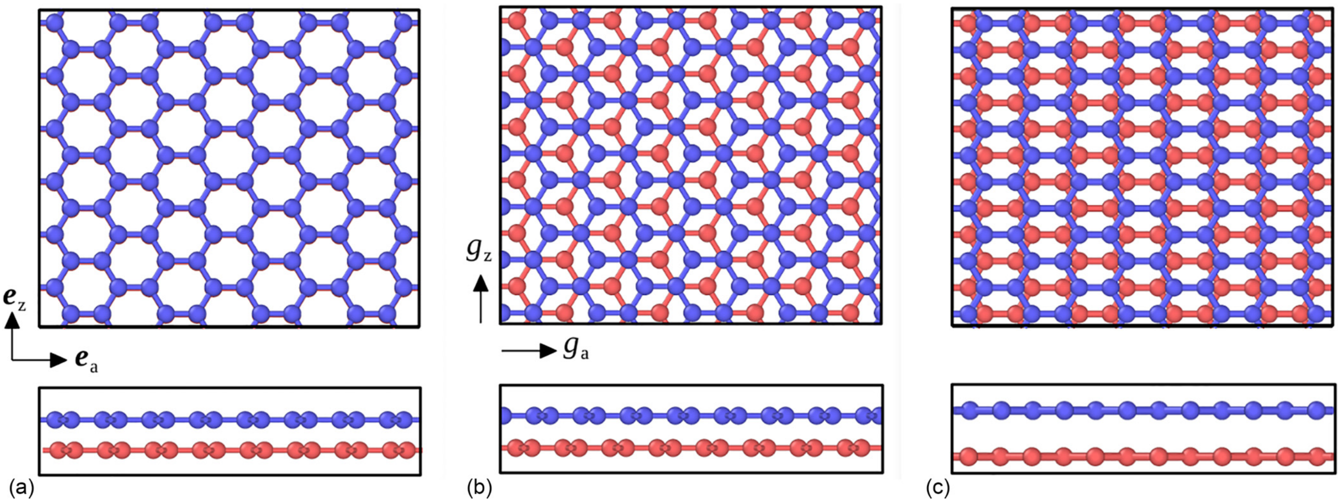

FIG. 1. Different stackings of bilayered graphene: (a) AA, (b) AB, and (c) SP stacking. g_a and g_z specify the relative displacement between the two sheets along the armchair and zigzag directions (denoted $\boldsymbol{e}_a$ and $\boldsymbol{e}_z$), respectively.

the surface area of a relaxed sheet, and $N = 4032$ is the total number of atoms of the top layer.

A timestep of 1 fs, suitable for the considered potentials [63], is employed to integrate the equations of motion by the velocity Verlet algorithm [64]. Periodic boundary conditions are employed along the $\boldsymbol{e}_a$ and $\boldsymbol{e}_z$ directions. All the MD simulations are performed using the Large-scale Atomic/Molecular Massively Parallel Simulator (LAMMPS) [65].

III. CONTINUUM INTERACTION MODEL

This section presents the proposed continuum contact interaction model for flat and curved graphene sheets following classical nonlinear contact formulations.

A. Interaction potential for flat bilayer graphene

For moderate contact pressures, mechanical dissipation is negligible and the surface interaction can be modeled using a surface potential. The interaction potential for two flat graphene sheets is commonly written in the form [2,66,67]

$$\Psi_{\text{flat}}(\boldsymbol{g}) = \Psi_1(g_n) + \Psi_2(g_n)\,\bar{\Psi}_t(g_a, g_z). \tag{2}$$

It gives the energy per undeformed area of a graphene unit cell interacting with an underlying graphene sheet. The gap vector $\boldsymbol{g}$ with components g_n, g_a, and g_z (see Fig. 2) admits any value, but the unit cell has to be aligned with the underlying sheet. An example for functions $\Psi_1(g_n)$, $\Psi_2(g_n)$, and $\bar{\Psi}_t(g_a, g_z)$ is given in Sec. IV. There $g_a = g_z = 0$ corresponds to the AA stack. Integrating (2) over the undeformed surface gives the total interaction energy

$$\Pi = \int_{\mathcal{S}} \Psi_{\text{flat}}\, dA. \tag{3}$$

This has to be equal for integration over top and bottom layer.

Remark III.1. Ψ_{flat} contains the atomic densities of the two sheets. By choice the density of the unit cell is taken as the initial density, such that Ψ_{flat} is the energy per initial area. The density of the lower sheet, however, should be taken as its current density, to account for the change in energy (and forces) due to deformation. Thus Ψ_{flat} depends on the area change of the neighboring sheet, J_ℓ, as described in Sauer and Wriggers [68]. For commensurate sheets the deformation in both sheets is equal, such that $J_2 = J_1$ and the integration equivalence of Eq. (3) is ensured. For incommensurate sheets potential (2) can be modified, see Remark IV.1. For small deformations, the dependency of Ψ_{flat} on J_ℓ and a resulting incommensurability can be neglected.

B. Interaction potential for curved bilayer graphene

Two curved graphene sheets, like the walls of two nested CNTs, have different surface area. Hence integral (3) will not be identical for both the walls unless the potential is modified. Integrating Eq. (2) over a common reference surface $\mathcal{S}_0$ yields

$$\Pi = \int_{\mathcal{S}_0} \Psi_{\text{flat}}\, dA_0. \tag{4}$$

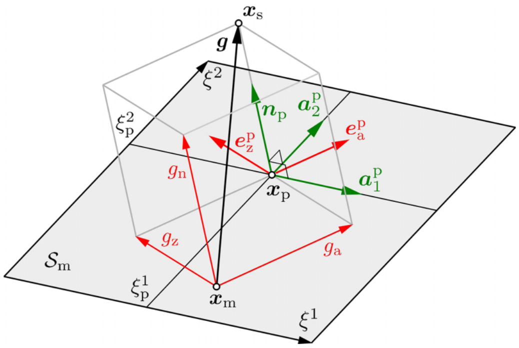

FIG. 2. Gap vector $\boldsymbol{g}$ between slave point $\boldsymbol{x}_s$ and master point $\boldsymbol{x}_m$ on $\mathcal{S}_m$, and its components g_n, g_a, and g_z. These are generally not equal to the surface coordinates ξ^1 and ξ^2 that are usually aligned with the surface geometry.

The curved area element dA_0 of the reference surface can be related to an aligned curved area element dA located at distance ξ_0 by

$$dA_0 = S(\xi_0)\,dA, \quad S(\xi_0) = 1 - 2H_0\,\xi_0 + \kappa_0\,\xi_0^2, \tag{5}$$

where H_0 and κ_0 are the mean and Gaussian curvature of dA, respectively. Their sign is defined with respect to the direction of positive ξ_0. Equation (5) is a well-known result from shell theory, e.g., see Başar and Ding [69] and Arciniega and Reddy [70]. Choosing the imaginary midsurface $\bar{\mathcal{S}}$ of the bilayer as the reference surface, which has the initial distance $G_n/2$ from either graphene layer, then gives

$$\Pi = \int_{\mathcal{S}} \Psi_c\,dA, \tag{6}$$

where

$$\Psi_c = \bar{S}\,\Psi_{\text{flat}}, \quad \bar{S} := S\left(\frac{G_n}{2}\right) = 1 - H_0\,G_n + \kappa_0\frac{G_n^2}{4}, \tag{7}$$

is the potential for a curved graphene unit cell above a graphene sheet.

As an example, consider two CNTs with radii $R_{\text{in}} = \bar{R} - G_n/2$ and $R_{\text{out}} = \bar{R} + G_n/2$, where $\bar{R}$ is the radius of the midsurface. In this case $H_{\text{in}} = -1/(2R_{\text{in}})$ and $H_{\text{out}} = +1/(2R_{\text{out}})$, while $\kappa_{\text{in}} = \kappa_{\text{out}} = 0$. Therefore, the value of $\bar{S}$ with respect to the outer and inner surfaces becomes $\bar{S}_{\text{in}} = \bar{R}/R_{\text{in}}$ and $\bar{S}_{\text{out}} = \bar{R}/R_{\text{out}}$, respectively, and the integration correctly yields

$$\Pi = \int_{\mathcal{S}_{\text{in}}} \Psi_c^{\text{in}}\,dA_{\text{in}} = \int_{\mathcal{S}_{\text{out}}} \Psi_c^{\text{out}}\,dA_{\text{out}} = \int_{\mathcal{S}_m} \Psi_{\text{flat}}\,\bar{R}\,d\theta\,dL, \tag{8}$$

for $\Psi_c^{\text{in}} = \bar{S}_{\text{in}}\,\Psi_{\text{flat}}$ and $\Psi_c^{\text{out}} = \bar{S}_{\text{out}}\,\Psi_{\text{flat}}$, since one can write $dA_{\text{in}} = R_{\text{in}}\,d\theta\,dL$ and $dA_{\text{out}} = R_{\text{out}}\,d\theta\,dL$, where L is the length of the CNT.

C. Contact kinematics

In frictional contact, the interaction of two surfaces depends on their relative normal and tangential displacement. This leads to the notion of a gap vector $\boldsymbol{g}$—with normal and tangential components—defined at every surface point. Following classical contact notation [44,45], the two interacting surfaces are distinguished into slave and master surface (see Fig. 2). Given the surface point $\boldsymbol{x}_s$ on the slave surface $\mathcal{S}_s$, its counterpart $\boldsymbol{x}_m$ on the neighboring master surface $\mathcal{S}_m$ is determined, as described below. The current contact gap then is

$$\boldsymbol{g} := \boldsymbol{x}_s - \boldsymbol{x}_m. \tag{9}$$

Given a parametrization of the master surface in the form

$$\boldsymbol{x}_m = \boldsymbol{x}_m(\xi^1, \xi^2), \tag{10}$$

one can determine the closest projection point $\boldsymbol{x}_p := \boldsymbol{x}_m(\xi_p^1, \xi_p^2)$ and its corresponding gap vector $\boldsymbol{g}_p := \boldsymbol{x}_s - \boldsymbol{x}_p$ by solving the two equations ($\alpha = 1, 2$),

$$\boldsymbol{g}_p \cdot \boldsymbol{a}_\alpha^p = 0, \tag{11}$$

for the local coordinates ξ_p^1 and ξ_p^2. Here

$$\boldsymbol{a}_\alpha^p := \frac{\partial \boldsymbol{x}_p}{\partial \xi_p^\alpha}, \quad \alpha = 1, 2, \tag{12}$$

denote the two tangent vectors of master surface $\mathcal{S}_m$ at point $\boldsymbol{x}_p$ along coordinates ξ^1 and ξ^2. Generally this is done by a local Newton-Raphson iteration for every $\boldsymbol{x}_s$ [45]. But for simple surfaces, such as cylinders, ξ_p^α can be determined in closed form, as discussed below. Given $\boldsymbol{x}_p$ the normal gap can then be determined from

$$g_n = \boldsymbol{g}_p \cdot \boldsymbol{n}_p, \tag{13}$$

where $\boldsymbol{n}_p$ is the surface normal of $\mathcal{S}_m$ at $\boldsymbol{x}_p$. The tangential gap, on the other hand, follows directly from the coordinates ξ_p^1 and ξ_p^2.

In the following examples the interaction of two nested CNTs during pull-out and twisting is considered. As deformations are expected to be small, the master surface is taken to be rigid (but movable), which simplifies the contact description greatly. The influence of this assumption on the sliding examples considered here is very small, as is seen later. The master surface thus is a rigid cylinder. The slave CNT and its surface point $\boldsymbol{x}_s$, on the other hand, are still considered general. The master CNT axis is denoted by vector $\boldsymbol{e}_1$, and vectors $\boldsymbol{e}_2$ and $\boldsymbol{e}_3$ span the cylinder cross section, see Fig. 3(a). Vectors $\boldsymbol{e}_i$ ($i = 1, 2, 3$) are taken as unit vectors and form a Cartesian basis. As Fig. 3(a) shows, coordinates ξ_p^1 and ξ_p^2 are considered aligned with the axial and circumferential direction, respectively. Either the inner CNT is the master surface and the outer CNT serves as slave (shown in red), or the outer CNT is the master surface and the inner CNT serves as slave (shown in blue). The axial projection point coordinate can then be written as

$$\xi_p^1 = \boldsymbol{x}_s \cdot \boldsymbol{e}_1 - u_m, \tag{14}$$

where u_m describes an axial rigid body displacement of the master surface. The circumferential projection point coordinate can be written as

$$\xi_p^2 = R_m\,\bar{\xi}_p^{\,2}, \quad \bar{\xi}_p^{\,2} = \operatorname{sgn}(\boldsymbol{n}_p \cdot \boldsymbol{e}_3)\,\arccos(\mp\boldsymbol{n}_p \cdot \boldsymbol{e}_2), \tag{15}$$

where R_m is the master cylinder radius and $\bar{\xi}_p^{\,2}$ is the circumferential angle. The upper sign in Eq. (15) corresponds to the case where the master cylinder is inside, while the lower sign is for the case where the master cylinder is outside, see Fig. 3(a). Axial rigid body rotations of the master cylinder are captured by a corresponding rotation of $\boldsymbol{e}_2$ and $\boldsymbol{e}_3$. The surface normal $\boldsymbol{n}_p$, needed for Eq. (15) can be determined from

$$\boldsymbol{n}_p = \pm\frac{\boldsymbol{P}(\boldsymbol{x}_s - \boldsymbol{x}_0)}{\|\boldsymbol{P}(\boldsymbol{x}_s - \boldsymbol{x}_0)\|}, \tag{16}$$

where $\boldsymbol{x}_0$ is some point on the cylinder axis and $\boldsymbol{P} := \boldsymbol{1} - \boldsymbol{e}_1 \otimes \boldsymbol{e}_1$ is a projection tensor. The sign in Eq. (16) follows the previous convention. Accordingly, $\boldsymbol{n}_p$ always points towards the other surface; see Fig. 3(a).

Given the quantities and sign convention in Eqs. (14)–(16), the normal gap follows as

$$g_n = \pm[\|\boldsymbol{P}(\boldsymbol{x}_s - \boldsymbol{x}_0)\| - R_m], \tag{17}$$

while the axial and circumferential gaps are

$$g^1 = \xi_p^1 - \xi_{p0}^1, \tag{18}$$

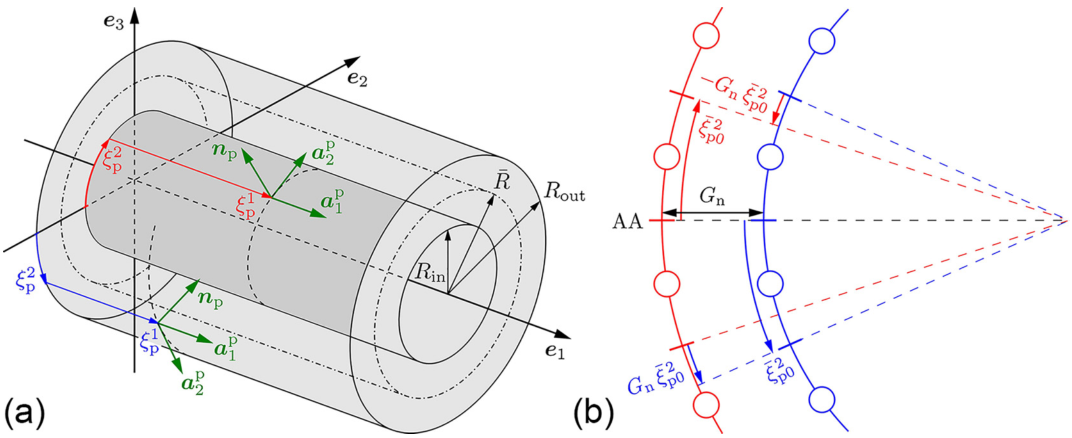

FIG. 3. Contact kinematics of interacting CNTs: (a) Coordinates ξ_p^α and master basis $\{\boldsymbol{a}_1^p, \boldsymbol{a}_2^p, \boldsymbol{n}_p\}$ on inner and outer CNT; normal vector $\boldsymbol{n}_p$ is chosen to point towards the neighboring slave CNT; ξ_p^2 and $\boldsymbol{a}_2^p$ thus point in opposite direction on both surfaces to ensure right-handed bases; (b) initial interference between inner and outer CNT with respect to the AA stack: The location $\bar{\xi}_{p0}^2$ on the inner CNT is ahead of the outer tube by the amount $G_n\,\bar{\xi}_{p0}^2$ (marked in blue), while the location $\bar{\xi}_{p0}^2$ on the outer CNT lags behind by the amount $G_n\,\bar{\xi}_{p0}^2$ (marked in red).

and

$$g^2 = \xi_p^2 - \xi_{p0}^2 \mp G_n\,\bar{\xi}_{p0}^2, \tag{19}$$

respectively. Here G_n and ξ_{p0}^α are the initial values of g_n and ξ_p^α that follow from Eqs. (14)–(16) for the initial (unrelaxed) location $\boldsymbol{X}_s$. The term $\xi_p^\alpha - \xi_{p0}^\alpha$ in Eqs. (18) and (19) describes relative tangential motion with respect to the initial state. The term $\mp G_n\,\bar{\xi}_{p0}^2$ in Eq. (19) is required in order to account for the circumferential lattice mismatch (i.e., lattice interference) between the two CNTs, as is illustrated in Fig. 3(b). Using the initial gap $G_n = R_{out} - R_{in}$ in Eq. (19) ensures that the interference is an integer multiple of the unit cell size, which in turn ensures periodicity in g^2. Figure 4 shows the initial tangential gaps g^1 and g^2 for CNT(15,15) inside CNT(20,20). Here g^1 arises due to the different stretching of the two CNTs—the inner tube is stretched and the outer shortens due to contact pressure—while g^2 is caused by the lattice mismatch term $\mp G_n\,\bar{\xi}_{p0}^2$. The former is negligible in comparison to the latter.

In the chosen parametrization given above, the tangent vector along ξ_p^1 and g^1 becomes

$$\boldsymbol{a}_1^p = \boldsymbol{e}_1, \tag{20}$$

while the tangent vector along ξ_p^2 and g^2 is

$$\boldsymbol{a}_2^p = \sin\bar{\xi}_p^2\,\boldsymbol{e}_2 \pm \cos\bar{\xi}_p^2\,\boldsymbol{e}_3. \tag{21}$$

Of these, only $\boldsymbol{a}_1^p$ is constant. But both $\boldsymbol{a}_1^p$ and $\boldsymbol{a}_2^p$ are normalized and orthogonal to each other. This implies that g^1 and g^2 measure the actual physical sliding distances. It also implies that the surface metric $a_{\alpha\beta}^p = \boldsymbol{a}_\alpha^p \cdot \boldsymbol{a}_\beta^p$ is equal to the Kronecker delta, i.e., the 2×2 matrix $[a_{\alpha\beta}^p]$ is the identity matrix.

In the above description, slave motions are captured through the motion of $\boldsymbol{x}_s$, leading to changed ξ_p^α and hence updated g^α. Master motion, on the other hand, is captured by changing ξ_p^α through changing u_m, $\boldsymbol{e}_2$, and $\boldsymbol{e}_3$.

The axial and circumferential gaps g^1 and g^2 are only aligned with the graphene lattice for armchair and zigzag CNTs. For general CNTs, described by the chirality parameters n and m and denoted CNT(n, m), the armchair and zigzag gaps are given by

$$\begin{aligned} g_a &= g^1\cos\theta + g^2\sin\theta, \\ g_z &= -g^1\sin\theta + g^2\cos\theta, \end{aligned} \tag{22}$$

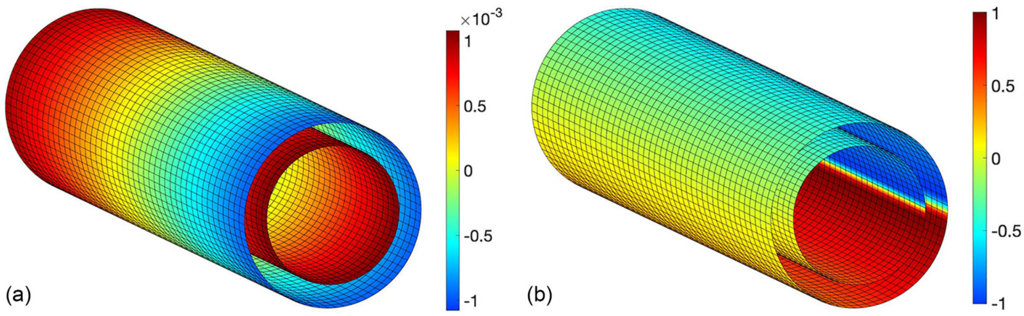

FIG. 4. Contact kinematics of interacting CNTs: Color plot of initial tangential gaps g^1 (a) and g^2 (b) in (nm) for relaxed CNT(15,15) inside relaxed CNT(20,20) with respect to the AA stack of the central cross-section. The initial CNT length is 9.9207 nm. g^1 has opposite sign on the two surfaces, as ξ_p^1 runs in the same direction on the two surfaces, see Fig. 3. It is the other way around for g^2.

with [71]

$$\cos\theta := \frac{2n+m}{2\sqrt{n^2+nm+m^2}}, \quad \sin\theta := \frac{\sqrt{3}\,m}{2\sqrt{n^2+nm+m^2}}. \tag{23}$$

The special case $m=0$ gives zigzag CNTs ($g_a = g^1$ and $g_z = g^2$), while $m = -2n$ gives armchair CNTs ($g_a = -g^2$ and $g_z = g^1$).

Introducing the matrices

$$[g^\alpha_{\mathrm{cc}}] := \begin{bmatrix} g_a \\ g_z \end{bmatrix}, \quad [Q^\alpha_{\ \beta}] := \begin{bmatrix} \cos\theta & \sin\theta \\ -\sin\theta & \cos\theta \end{bmatrix}, \tag{24}$$

and defining $\bar\xi^1_{p0} := 0$ allows us to simplify Eqs. (18), (19), and (22) into[3]

$$g^\alpha_{\mathrm{cc}} = Q^\alpha_{\ \beta}\, g^\beta, \quad g^\beta = \xi^\beta_p - \xi^\beta_{p0} \mp G_n\,\bar\xi^\beta_{p0}. \tag{25}$$

Note that components $Q^\alpha_{\ \beta}$ need to be distinguished from the components $Q_\beta^{\ \alpha}$ of the transpose matrix $[Q_\beta^{\ \alpha}] = [Q^\alpha_{\ \beta}]^T$ appearing in

$$g^\alpha = Q_\beta^{\ \alpha}\, g^\beta_{\mathrm{cc}}. \tag{26}$$

For the derivation of the contact tractions (and their subsequent linearization) the kinematical quantities above need to be differentiated with respect to surface changes. If only the slave surface is deformable, as is considered here, then only the gradients with respect to slave point $\boldsymbol{x}_s$ are needed. From Eqs. (13) and (25) follow

$$\frac{\partial g_n}{\partial \boldsymbol{x}_s} = \boldsymbol{n}_p \tag{27}$$

and

$$\frac{\partial g^\alpha_{\mathrm{cc}}}{\partial \boldsymbol{x}_s} = Q^\alpha_{\ \beta}\, \frac{\partial \xi^\beta_p}{\partial \boldsymbol{x}_s}, \tag{28}$$

since θ, G_n, and $\bar\xi^\beta_{p0}$ are constant. From Eqs. (14), (20), (15), and (16) follow after some steps,

$$\frac{\partial \xi^1_p}{\partial \boldsymbol{x}_s} = \boldsymbol{a}^p_1, \quad \frac{\partial \xi^2_p}{\partial \boldsymbol{x}_s} = \frac{R_m}{R_m \pm g_n}\boldsymbol{a}^p_2, \tag{29}$$

or

$$\frac{\partial \xi^\alpha_p}{\partial \boldsymbol{x}_s} = c^{\alpha\beta}\,\boldsymbol{a}^p_\beta, \quad [c^{\alpha\beta}] := \begin{bmatrix} 1 & 0 \\ 0 & \dfrac{R_m}{R_m \pm g_n} \end{bmatrix}. \tag{30}$$

These expressions are consistent with standard contact formulas, e.g., see Wriggers [45] and Sauer and De Lorenzis [72]. Inserting (30) into (28) gives

$$\frac{\partial g^\alpha_{\mathrm{cc}}}{\partial \boldsymbol{x}_s} = Q_c^{\alpha\gamma}\,\boldsymbol{a}^p_\gamma, \tag{31}$$

with

$$Q_c^{\alpha\gamma} := Q^\alpha_{\ \beta}\, c^{\beta\gamma}. \tag{32}$$

D. Contact tractions

The contact traction at slave surface point $\boldsymbol{x}_s$ is given by

$$\boldsymbol{t}_s := -\frac{\partial \Psi_c}{\partial \boldsymbol{x}_s} = -\frac{\partial \Psi_c}{\partial g_n}\frac{\partial g_n}{\partial \boldsymbol{x}_s} - \frac{\partial \Psi_c}{\partial g^\alpha_{\mathrm{cc}}}\frac{\partial g^\alpha_{\mathrm{cc}}}{\partial \boldsymbol{x}_s}. \tag{33}$$

Inserting Eq. (27) and Eq. (31), leads to

$$\boldsymbol{t}_s = p\,\boldsymbol{n}_p + t^\gamma\,\boldsymbol{a}^p_\gamma, \tag{34}$$

with the contact pressure

$$p := -\frac{\partial \Psi_c}{\partial g_n} \tag{35}$$

and tangential contact traction

$$t^\gamma = t^c_\alpha\, Q_c^{\alpha\gamma}, \tag{36}$$

based on

$$t^c_\alpha := -\frac{\partial \Psi_c}{\partial g^\alpha_{\mathrm{cc}}}. \tag{37}$$

Here t^1 and t^2 are the traction components in axial and circumferential direction, while t^c_1 and t^c_2 are the traction components in armchair and zigzag direction, respectively. According to Eq. (34), all components of $\boldsymbol{t}_s$ are expressed in the master basis $\{\boldsymbol{a}^p_1, \boldsymbol{a}^p_2, \boldsymbol{n}_p\}$. From Eq. (7) and Eq. (2) then follows

$$p = \bar S\,(p_1 + p_2\bar\Psi_t), \tag{38}$$

for

$$p_1 := -\frac{\partial \Psi_1}{\partial g_n}, \quad p_2 := -\frac{\partial \Psi_2}{\partial g_n}, \tag{39}$$

and

$$t^c_\alpha = \bar S\,\Psi_2\,\bar t^c_\alpha, \tag{40}$$

for

$$\bar t^c_\alpha := -\frac{\partial \bar\Psi_t}{\partial g^\alpha_{\mathrm{cc}}}. \tag{41}$$

Note that expression (36) can also be written as $t^\gamma = Q_{cT}^{\gamma\alpha}\, t^c_\alpha$ with $[Q_{cT}^{\alpha\beta}] := [Q_c^{\alpha\beta}]^T$. Analogously to Eq. (24.1), we will also use

$$[\bar t^c_\alpha] =: \begin{bmatrix} \bar t_a \\ \bar t_z \end{bmatrix}. \tag{42}$$

IV. CONTINUUM MODEL CALIBRATION

The continuum description in Sec. III is for general $\Psi_1(g_n)$, $\Psi_2(g_n)$, and $\bar\Psi_t(g_a, g_z)$. Now specific choices for these functions are considered and calibrated from MD data for moderate contact pressures, where dissipation is negligible. At large contact pressures, mechanical energy is dissipated, and the proposed model becomes insufficient, as is shown in Sec. IV D.

A. Potential functions

Considering

$$\Psi_1(g_n) = p_{01}\, g_{01}\left[\frac{1}{10}\left(\frac{g_{01}}{g_n}\right)^{10} - \frac{1}{4}\left(\frac{g_{01}}{g_n}\right)^{4}\right] \tag{43}$$

---

[3] Here and in the following, summation is implied on repeated Greek indices according to the rules of index notation.

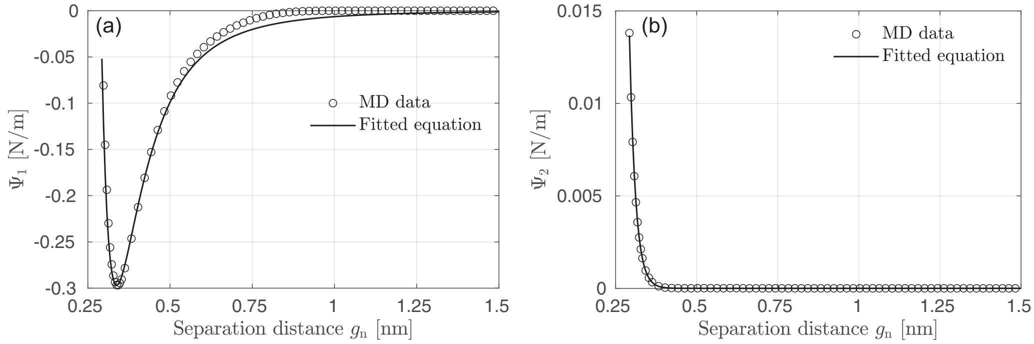

FIG. 5. Calibrated potential functions $\Psi_1(g_n)$ (a) and $\Psi_2(g_n)$ (b) using the shown MD data. The MD data for Ψ_1 is obtained at $g_a = 3a_{\rm cc}/8$ and $g_z = \sqrt{3}a_{\rm cc}/4$, while the MD data for Ψ_2 is averaged over several g_a and g_z values.

leads to

$$p_1 = p_{01}\left[\left(\frac{g_{01}}{g_n}\right)^{11} - \left(\frac{g_{01}}{g_n}\right)^{5}\right], \tag{44}$$

according to Eq. (39.1), and

$$p_1' := \frac{\partial p_1}{\partial g_n} = -\frac{p_{01}}{g_{01}}\left[11\left(\frac{g_{01}}{g_n}\right)^{12} - 5\left(\frac{g_{01}}{g_n}\right)^{6}\right], \tag{45}$$

while the ansatz

$$\Psi_2(g_n) := p_{02}\, g_{02} \exp\left(-\frac{g_n}{g_{02}}\right) \tag{46}$$

gives

$$p_2 = p_{02} \exp\left(-\frac{g_n}{g_{02}}\right), \tag{47}$$

according to Eq. (39.2) and

$$p_2' := \frac{\partial p_2}{\partial g_n} = -\frac{p_{02}}{g_{02}} \exp\left(-\frac{g_n}{g_{02}}\right). \tag{48}$$

Here p_{01}, g_{01}, p_{02}, and g_{02} are constants that are calibrated from MD simulations, which is discussed subsequently. The potential $\Psi_1(g_n)$ specifies the mean of the interaction energy. The widely used surface-integrated LJ potential is chosen for $\Psi_1(g_n)$ [18,73,74]. Our proposed potential $\Psi_2(g_n)$, on the other hand, is solely motivated from the obtained MD data.

Further, the tangential potential [2,66,67]

$$\bar{\Psi}_t(g_a, g_z) = \cos\frac{4\pi g_a}{\ell_a} + 2\cos\frac{2\pi g_a}{\ell_a}\cos\frac{2\pi g_z}{\ell_z} \tag{49}$$

yields

$$\bar{t}_a = -\frac{\partial\bar{\Psi}_t}{\partial g_a} = \frac{4\pi}{\ell_a}\left(\sin\frac{4\pi g_a}{\ell_a} + \sin\frac{2\pi g_a}{\ell_a}\cos\frac{2\pi g_z}{\ell_z}\right),$$

$$\bar{t}_z = -\frac{\partial\bar{\Psi}_t}{\partial g_z} = \frac{4\pi}{\ell_z}\cos\frac{2\pi g_a}{\ell_a}\sin\frac{2\pi g_z}{\ell_z}, \tag{50}$$

and

$$\begin{aligned}\frac{\partial\bar{t}_a}{\partial g_a} &= \frac{8\pi^2}{\ell_a^2}\left(2\cos\frac{4\pi g_a}{\ell_a} + \cos\frac{2\pi g_a}{\ell_a}\cos\frac{2\pi g_z}{\ell_z}\right),\\ \frac{\partial\bar{t}_a}{\partial g_z} &= \frac{\partial\bar{t}_z}{\partial g_a} = -\frac{8\pi^2}{\ell_a\,\ell_z}\sin\frac{2\pi g_a}{\ell_a}\sin\frac{2\pi g_z}{\ell_z},\\ \frac{\partial\bar{t}_z}{\partial g_z} &= \frac{8\pi^2}{\ell_z^2}\cos\frac{2\pi g_a}{\ell_a}\cos\frac{2\pi g_z}{\ell_z}.\end{aligned} \tag{51}$$

Here ℓ_a and ℓ_z are treated as constants that follow from the graphene lattice, see Table I, and g_a and g_z are the relative displacement components between two graphene layers along the armchair and zigzag directions, respectively. Thus, function $\bar{\Psi}_t$ is fully specified and only Ψ_1 and Ψ_2 remain to be calibrated.

Remark IV.1. If the neighboring graphene lattice deforms, ℓ_a and ℓ_z are not constant anymore. Stretches along armchair and zigzag direction can be accounted for in Eq. (49) by writing

$$\ell_a = \lambda_a L_a, \quad \ell_z = \lambda_z L_z, \tag{52}$$

where L_a and L_z are the initial lattice periods. In the small deformation regime, the stretches are related to the corresponding infinitesimal strains by

$$\lambda_a = 1 + \varepsilon_a, \quad \lambda_z = 1 + \varepsilon_z. \tag{53}$$

Shear strains ε_{az} are not accounted for in these expressions. It can be expected that they require changes of the functional form in Eq. (49).

TABLE I. Potential parameters.

Parameters	Value
$a_{\rm cc}$	0.1397 nm
$\bar{l}_a$	3
$\bar{l}_z$	$\sqrt{3}$
l_a	$\bar{l}_a\, a_{\rm cc}$
l_z	$\bar{l}_z\, a_{\rm cc}$
p_{01}	5.8646 nN/nm^2
g_{01}	0.3376 nm
p_{02}	4.404×10^6 nN/nm^2
g_{02}	1.875×10^{-2} nm

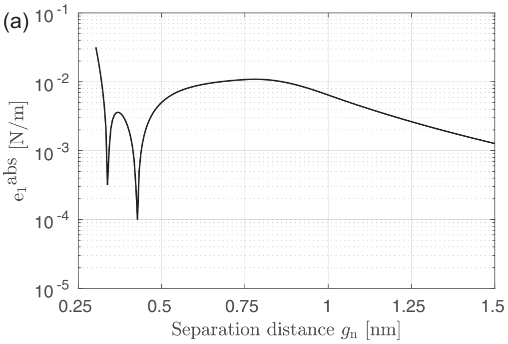

FIG. 6. (a) Absolute and (b) relative error of Ψ_1 as a function of separation distance g_n.

B. Potential calibration

To calibrate the potential parameters in Eq. (43), the top layer is displaced by $g_a = 3a_{cc}/8$ and $g_z = \sqrt{3}a_{cc}/4$, and the interaction energy Ψ_{flat} between the two graphene sheets is recorded for varying g_n from MD simulations. For the selected values of g_a and g_z, the tangential potential $\bar{\Psi}_t$ is zero such that the interaction energy is equal to Ψ_1. The parameters of Eq. (43) are then fitted to the obtained data using least-squares curve fitting; see Fig. 5(a). The calibrated parameters thus become $g_{01} = 0.3376$ nm and $p_{01} = 5.8646$ nN/nm^2.

In order to determine the constants in Eq. (46), we choose different combinations of g_a and g_z and determine Ψ_{flat} from MD simulations for varying g_n. The values of g_a and g_z are varied over one period, respectively (see Fig. 1). The potential Ψ_2 then follows as $(\Psi_{flat} - \Psi_1)/\bar{\Psi}_t$, according to Eq. (2). For each g_n, the Ψ_2 data are averaged for all g_a and g_z values and then used to calibrate the parameters of Eq. (46) using least-squares curve fitting. This gives $p_{02} = 4.404 \times 10^6$ nN/nm^2 and $g_{02} = 1.875 \times 10^{-2}$ nm. The two calibrated functions Ψ_1 and Ψ_2 are shown in Fig. 5.

To check the accuracy of Ψ_1, the absolute and relative errors of function $\Psi_1(g_n)$ with respect to the MD data Ψ_1^{MD} are calculated from $e_1^{abs} = |\Psi_1^{MD} - \Psi_1|$ and $e_1^{rel} = e_1^{abs}/|\Psi_1|$, respectively, and shown in Fig. 6. As seen, the absolute difference is less than 3×10^{-2} N/m. The relative error approaches one as g_n increases, since Ψ_1^{MD} reaches approximately zero for $g_n > 1$ nm. All potential parameters are summarized in Table I.

C. Resulting interaction behavior

The continuum model has been calibrated by fitting functions Ψ_1 and Ψ_2 for selected g_a and g_z values. We now show that this is sufficient to describe energy Ψ_{flat} and its resulting contact tractions $\boldsymbol{t}_t$ and p over a wide range of separation distances.

1. Potential energy

Figure 7 shows that the interaction energies determined from the MD simulations and continuum model are in good agreement across the entire range of g_a and g_z, with an average absolute error of ≈3%. Here the MD results are based on the LJ potential for the interaction between the graphene layers. A comparison to other interaction potentials is discussed in Appendix A. The three sliding paths shown in Fig. 7 are examined next. They are kept straight in order to sample all energy levels.[4]

Figure 8(a) shows the interaction energy Ψ_{flat} as a function of relative armchair displacement g_a for $g_z = 0$. The separation distance between the two sheets is taken as $g_n = 0.3366$ nm, which corresponds to the equilibrium separation distance of the AB stacking. The maxima of Ψ_{flat} vs g_a are located at $g_a = 0$ and multiples of ℓ_a, which all correspond

---

[4] If lateral motions are allowed, the sliding trajectory will follow the minimum energy paths along the blue valleys [75].

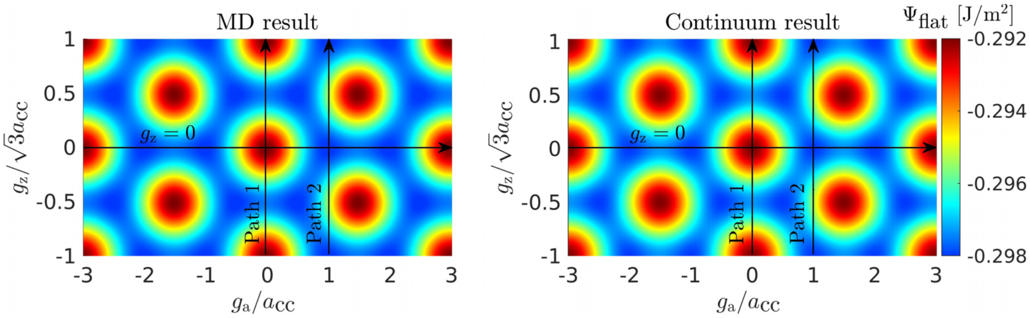

FIG. 7. Variation of interaction energy Ψ_{flat} obtained from MD simulations and continuum model. Three sliding paths are investigated: The armchair path at $g_z = 0$ and two sliding paths at $g_a = 0$ and $g_a = a_{cc}$.

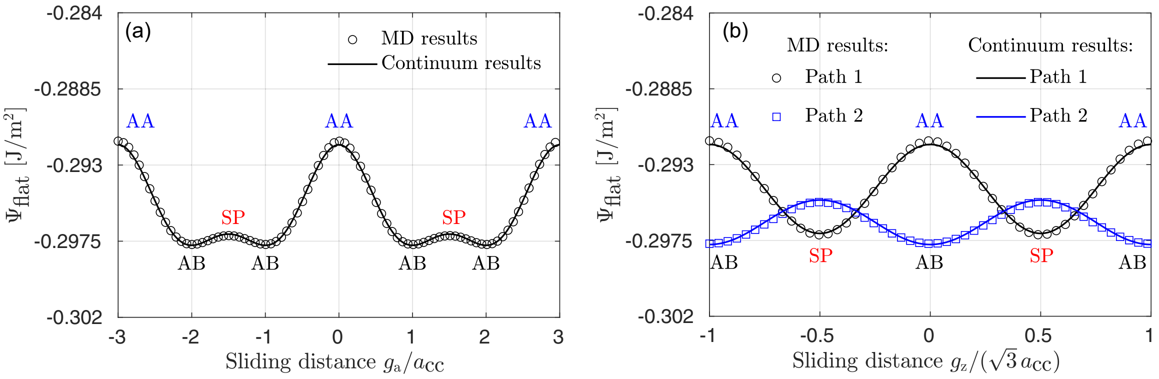

FIG. 8. Variation of interaction energy Ψ_{flat}: Sliding along the (a) armchair path and (b) two zigzag paths shown in Fig. 7, all at $g_n = 0.3366$ nm (∼ equilibrium separation distance of the AB stacking). The difference between (a) and (b) illustrates the sliding anisotropy.

to the AA stacking. The global minima and local maxima are located at $g_a = \pm a_{\text{cc}}$, $g_a = \pm 2a_{\text{cc}}$, and $g_a = \pm 1.5a_{\text{cc}}$, which are the AB and SP stackings, respectively. This is in agreement with experimental studies [12]. The binding energy of bilayer graphene at the equilibrium separation distance of the AB stacking is -46.9 meV/atom,[5] agreeing with the value -45.6 meV/atom from Lebedeva *et al.* [35]. The slight difference can be attributed to the elastic nature of the sheet, as well as the accuracy of the interatomic potential functions and the constants used. Further, the amplitude of Ψ_{flat}, obtained as $\Delta\Psi^{\text{AA}}_{\text{flat}} = \Psi^{\text{AA}}_{\text{flat}} - \Psi^{\text{AB}}_{\text{flat}}$, is 6.129×10^{-3} N/m, and the amplitude between the AB and SP stacking is $\Delta\Psi^{\text{SP}}_{\text{flat}} = \Psi^{\text{SP}}_{\text{flat}} - \Psi^{\text{AB}}_{\text{flat}} = 6.770 \times 10^{-4}$ N/m.

Figure 8(b) shows the interaction energy Ψ_{flat} as a function of the relative zigzag displacement g_z for $g_a = 0$ (Path 1) and $g_a = a_{\text{cc}}$ (Path 2). The maxima of Ψ_{flat} vs g_z for Path 1 are located at $g_a = 0$ and multiples of ℓ_z, which all correspond to the AA stacking, while the minima are at $g_a = \pm\ell_z/2$, which correspond to the SP stacking. For Path 2, the minima correspond to the AB stacking.

2. Tangential traction

For flat graphene sheets, the expressions in Sec. III D simplify to the tangential traction

$$\boldsymbol{t}_t = \Psi_2\left(\bar{t}_a\,\boldsymbol{e}_a + \bar{t}_z\,\boldsymbol{e}_z\right), \tag{54}$$

where $\bar{t}_a$ and $\bar{t}_z$ are given by Eq. (50) and Ψ_2 was calibrated above. Figures 9(a) and 9(b) show the comparison of these tractions with those determined from the MD simulations considering sliding along the armchair direction (for $g_z = 0$) and zigzag direction (for Path 1 and Path 2), respectively. As seen, the continuum tractions agree well with those obtained from the MD simulations across the entire range of sliding distances, with an average error of ≈3%.

The amplitude of the tangential traction, calculated as $t_s^{\max} - t_s^{\min}$, where subscript s denotes the sliding direction, is 0.1460 N/m for the path in Fig. 9(a), which reduces by ≈1.2% and ≈55% for the two zigzag paths shown in Fig. 9(b). Further, the amplitude of the sticking limit, i.e., $t_s^{\max} - t_s^{\min}$ depends on the separation distance g_n (or normal pressure), as Fig. 10 shows. In all three cases, the sticking limit decays exponentially with increasing separation gap.

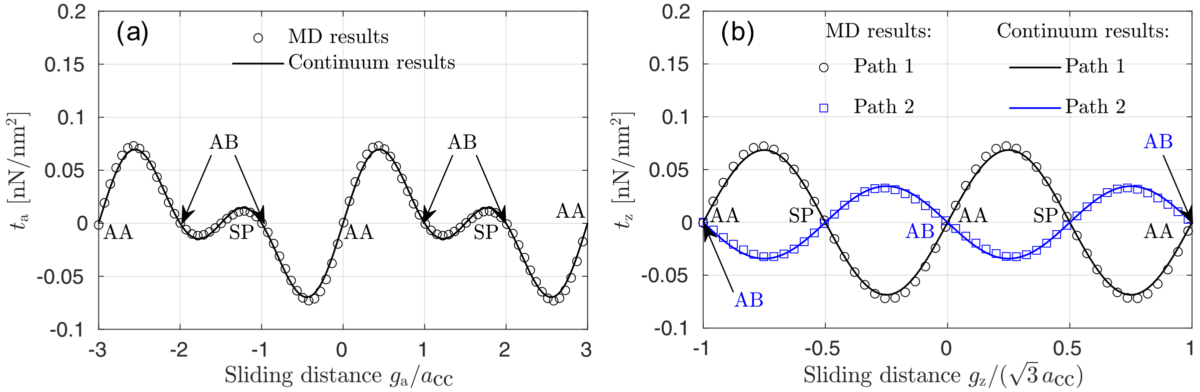

FIG. 9. Tangential traction: Sliding along the (a) armchair direction for $g_z = 0$ and (b) zigzag direction for $g_a = 0$ (Path 1) and $g_a = a_{\text{cc}}$ (Path 2), all at $g_n = 0.3366$ nm (∼ equilibrium separation distance of AB stacking). The difference between (a) and (b) illustrates the sliding anisotropy.

---

[5] The binding energy of bilayer graphene in meV/atom is calculated by normalizing the total interaction energy by the total number of atoms. 1 J/m^2 = 0.15758 eV.

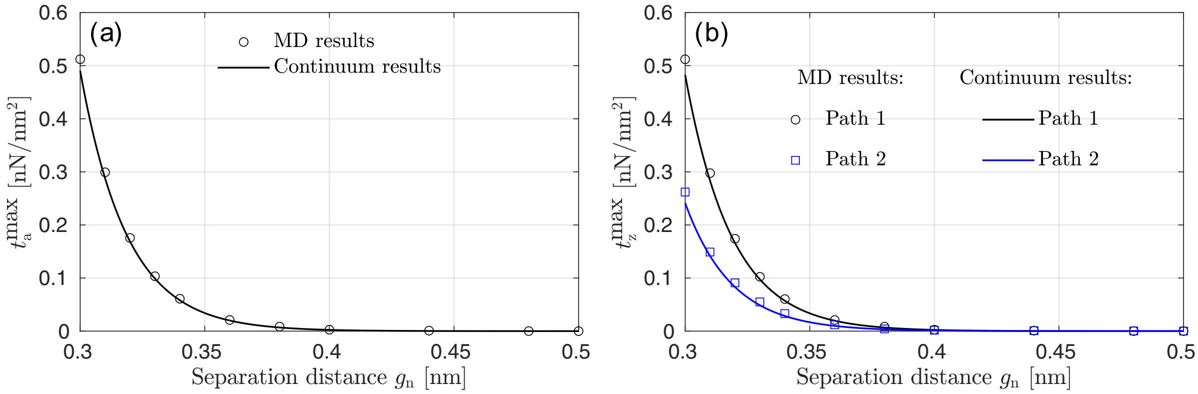

FIG. 10. Maximum tangential traction (= sticking limit) at different separation distances for sliding along the (a) armchair direction for $g_z = 0$ and (b) zigzag direction for $g_a = 0$ (Path 1) and $g_a = a_{\text{cc}}$ (Path 2).

3. *Normal traction*

For flat graphene sheets, the expression in Eq. (47) simplifies to the contact pressure (i.e., normal traction)

$$p = p_1 + \bar{\Psi}_t\, p_2, \tag{55}$$

which is specified through Eqs. (44), (47), and (49) and Table I. The value of $\bar{\Psi}_t(g_a, g_z)$ in Eq. (55) for the three stackings is $\bar{\Psi}_t^{\text{AA}} = 3$, $\bar{\Psi}_t^{\text{AB}} = -1.5$, and $\bar{\Psi}_t^{\text{SP}} = -1$. The comparison of the continuum and MD results for $p(g_n)$ is shown in Fig. 11(a), while Fig. 11(b) shows the absolute error defined as $e_p^{\text{abs}} = |p^{\text{MD}} - p|$. The normal traction depends not only on the separation distance between the two layers but also on the type of stacking. At $g_n = 0.3$ nm, p equals ≈11.8 nN/nm^2 for the AA stacking. At the same g_n, these values are ≈15.8% and ≈10.9% less for the AB and SP stackings, respectively, compared to the AA stacking. The equilibrium separation distances are 0.3394, 0.3366, and 0.3370 nm for the AA, AB, and SP stackings, and Eq. (55) captures this behavior sufficiently well, as Fig. 11 shows.

D. High-pressure limitation

The calibration of the continuum model assumes small in-plane deformations of the graphene layers, which is accurate for separation distances larger than 0.29 nm. For $g_n < 0.29$ nm, the contact pressure becomes very large, leading to nonuniform tangential deformations in the graphene layer as observed in MD simulations[6] [see Fig. 12(a)]. As a result, the bilayer graphene system attains different stackings in different regions. As Fig. 12(a) shows, the center of the sheet is in the AB stacking while the edges remain in the AA stacking. This tangential deformation is solely a result of the large contact pressure, as no tangential displacements are applied to the boundary in this case. As a consequence of the tangential displacements at the center, energy is dissipated when additional tangential displacements are applied to the boundary. Figure 12(b) therefore shows the amount of heat exchanged with the thermostat, Q, as a function of the sliding distance along the armchair direction (for $g_z = 0$ and various values for g_n). As seen in the figure, for $g_n \leqslant 0.28$ nm Q increases sharply for every $3a_{\text{cc}}$ of sliding distance. The increase is constant for fixed g_n. Each increase corresponds to a sudden release of the strain energy in the two layers. Since the energy remains constant after each increase, it implies that energy is lost to the heat bath. This mechanical dissipation mechanism is not accounted for in the present continuum model. The present continuum model, which is conservative, is therefore only valid for $g_n \geqslant 0.29$ nm.

---

[6] At each applied pressure level, the system is relaxed using the Polak-Ribiere conjugate gradient method followed by thermal equilibration employing the Nosé-Hoover thermostat.

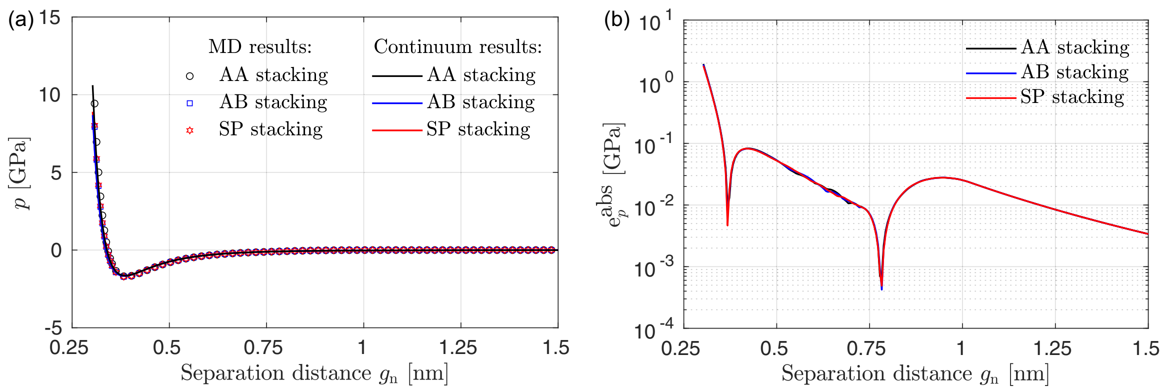

FIG. 11. (a) Contact pressure or normal traction (t_n) and (b) absolute error of t_n as a function of separation distance for the three stackings.

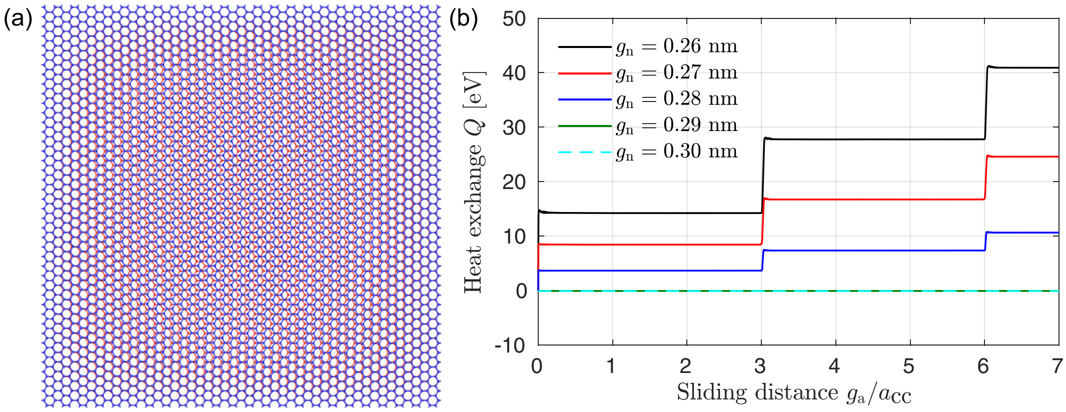

FIG. 12. Transition from dissipative to nondissipative sliding friction: (a) Bilayer configuration at $g_a = 0$, $g_z = 0$, and $g_n = 0.26$ nm. (b) Thermal energy exchange with the heat bath at different g_n for sliding along the armchair direction (for $g_z = 0$). The figure shows that sliding contact becomes nondissipative at $g_n \geqslant 0.29$ nm.

V. FINITE-ELEMENT FORMULATION

The calibrated continuum interaction model can be implemented straightforwardly within a nonlinear finite-element contact code. The contact traction from Eq. (34) and its gradient in Eq. (C11) enter the finite-element contact force vector

$$\mathbf{f}_c^e = -\int_{\Omega_0^e} \mathbf{N}_e^T\, \boldsymbol{t}_s\, dA, \tag{56}$$

and its associated stiffness matrix,

$$\mathbf{k}_c^e = -\int_{\Omega_0^e} \mathbf{N}_e^T\, \frac{\partial \boldsymbol{t}_s}{\partial \boldsymbol{x}_s}\, \mathbf{N}_e\, dA \tag{57}$$

[68,76]. Vector $\mathbf{f}_c^e$ acts on the FE nodes of the slave surface and is integrated over the reference slave element domain Ω_0^e in accordance to the integration defined in Eq. (6). Elemental array $\mathbf{N}_e := [\mathbf{1}N_1,\ \mathbf{1}N_2, \ldots,\ \mathbf{1}N_{n_e}]$, where $\mathbf{1}$ is the 3×3 identity tensor, contains the n_e nodal shape functions N_I that discretize the current and reference geometry according to

$$\boldsymbol{x} \approx \sum_I^{n_e} N_I\, \boldsymbol{x}_I = \mathbf{N}_e\, \mathbf{x}_e, \quad \boldsymbol{X} \approx \sum_I^{n_e} N_I\, \boldsymbol{X}_I = \mathbf{N}_e\, \mathbf{X}_e, \tag{58}$$

and the displacement field,

$$\boldsymbol{u} := \boldsymbol{x} - \boldsymbol{X} \approx \sum_I^{n_e} N_I\, \boldsymbol{u}_I = \mathbf{N}_e\, \mathbf{u}_e, \tag{59}$$

within each element e. Here

$$\mathbf{x}_e := \begin{bmatrix} \boldsymbol{x}_1 \\ \boldsymbol{x}_2 \\ \vdots \\ \boldsymbol{x}_{n_e} \end{bmatrix}, \quad \mathbf{X}_e := \begin{bmatrix} \boldsymbol{X}_1 \\ \boldsymbol{X}_2 \\ \vdots \\ \boldsymbol{X}_{n_e} \end{bmatrix}, \quad \mathbf{u}_e := \begin{bmatrix} \boldsymbol{u}_1 \\ \boldsymbol{u}_2 \\ \vdots \\ \boldsymbol{u}_{n_e} \end{bmatrix},$$
$$\boldsymbol{u}_I = \boldsymbol{x}_I - \boldsymbol{X}_I, \tag{60}$$

denote the arrays of all n_e nodal positions and displacements of element e. The elemental contributions $\mathbf{f}_c^e$ and $\mathbf{k}_c^e$ are assembled in the global arrays $\mathbf{f}_c$ and $\mathbf{k}_c$ that enter the discretized weak form and its linearization, which is required for a global Newton-Raphson solution procedure. In the present formulation the master surface is treated rigidly (but movable). Hence only the deformation of the slave surface is discretized and computed by FE. Alternating the designation of master and slave surface then allows to asses the error of treating the master surface rigidly. For the following examples, the preceding equations have been implemented in the isogeometric shell finite-element formulation of Duong *et al.* [77] and Ghaffari *et al.* [78] using the contact interaction formulation of Sauer and De Lorenzis [72,79].

VI. APPLICATION EXAMPLES: CNT PULL-OUT AND TWISTING

We now turn to a set of application examples for validating the proposed continuum model. Considered is a CNT that is either pulled-out from or twisted within a second CNT.

TABLE II. Geometric parameters of inner and outer CNTs of DWCNTs before relaxation.

	Inner CNT		Outer CNT		Radial gap	Length (L)	
Case	Chirality	R_i (nm)	Chirality	R_o (nm)	(G_n) (nm)	Unit cells	(nm)
1	(26,0)	1.0013	(35,0)	1.3479	0.3466	24	10.0584
2	(15,15)	1.0005	(20,20)	1.3340	0.3335	42	10.1626
3	(21,9)	1.0269	(28,12)	1.3691	0.3423	3	11.1751

TABLE III. Geometric parameters of inner and outer CNTs of DWCNTs after individual and combined relaxation. The geometry parameters after relaxation are denoted with lowercase letters.

	Individual CNT relaxation				Combined DWCNT relaxation			
Case	r_i (nm)	r_o (nm)	g_n (nm)	$\frac{(\ell_i+\ell_o)}{2}$ (nm)	r_i (nm)	r_o (nm)	g_n (nm)	ℓ (nm)
1	1.0026	1.3487	0.3461	10.0611	1.0036	1.3466	0.3430	10.0573
2	1.0014	1.3345	0.3331	10.1694	0.9997	1.3362	0.3366	10.1638
3	1.0279	1.3698	0.3419	11.1803	1.0281	1.3689	0.3410	11.1766

A. CNT geometry and loading

1. Initial CNT geometry

The following three cases of DWCNTs are considered for pull-out and twisting:

(1) CNT (26,0) inside CNT(35,0)
(2) CNT (15,15) inside CNT(20,20)
(3) CNT (21,9) inside CNT(28,12)

The initial geometry parameters of these three cases, such as inner and outer CNT radii (R_i and R_o), radial separation gap G_n, and length L are listed in Table II. The initial radius [71] of an undeformed CNT is given by

$$R = (\sqrt{3}a_{\mathrm{cc}}/2\pi)\sqrt{n^2+m^2+nm}, \tag{61}$$

where n and m are the chirality indices [71]. A schematic representation of the setup is shown in Fig. 13.

Initially, the CNTs are relaxed following the approach described in Sec. II. The geometry parameters of three cases of CNTs after individual and combined relaxation are given in Table III. As discussed earlier, the equilibrium separation distance between two graphene layers depends on their stacking. Due to the curvature, DWCNTs possess various stackings, which implies that the contact pressure between the CNTs is not constant, and the CNT radii thus vary across the surface. Table III reports the average radii. Table III also shows that the average gap $g_n = r_o - r_i$ is either in a state of attraction (for Case 1 and 3) or in a state of repulsion (for Case 2). The three cases thus cover negative and positive contact pressures between the walls. Comparison between Tables II and III shows that the inner radius increases and the outer radius decreases for Case 1 and 3, while it is the other way around for Case 2. This is due to the positive Poisson ratio of graphene (see Appendix B): Positive contact pressure leads to circumferential strains that are positive in the outer tube and negative in the inner tube. These circumferential strains lead to axial strains that are negative for the outer tube and positive for the inner tube. For negative contact stresses, the effect is reversed.

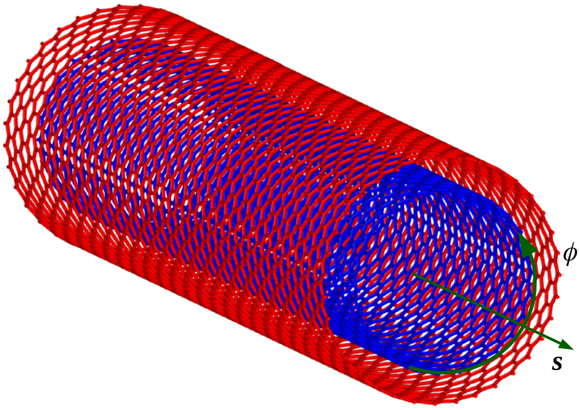

FIG. 13. Schematic representation of the pull-out and twisting of an inner CNT from/within an outer CNT. Shown here are CNT(26,0) and CNT(35,0).

2. Load application in MD

After obtaining the relaxed DWCNTs, the inner CNT is pulled quasi-statically by assigning the velocity 0.001 Å/ps to the right edge atoms (see Fig. 13). For twisting, the right edge atoms of the inner CNT are rotated with an angular velocity of 6.28×10^{-4} rad/ps. During pull-out or twisting, atoms on the left edge of the outer CNT and those on the right edge of the inner CNT are constrained in the tangential direction employing a torsional spring with stiffness 16.02 nN-nm/rad. Thus, a radial expansion of the CNTs is allowed. The resisting pull-out force is then calculated as the total vdW force in axial direction acting on the inner CNT due to the outer CNT. The torque is calculated as $\sum_{I=1}^{N}[F_I^y\cos(\phi) - F_I^x\sin(\phi)]r$, where F_I^x and F_I^y are the inter-CNT vdW force components acting on atom I along the x and y directions, respectively. Here r is the radius, ϕ is its angle of twist, and N is its total number of atoms of the CNT.

3. Load application in FE

For pull-out, a constant displacement is prescribed to all FE nodes of the central cross-section of the CNT, while the rotation is constrained, but lateral motions are allowed, such that the lateral forces on the tubes remain zero. The tubes therefore do not remain exactly concentric during pull-out. For twisting, a constant rotation is applied by moving all atoms of the central cross section in circumferential direction, while keeping the radial direction free. The longitudinal direction remains fixed during the rotation.

The FE simulations show that enforcing concentricity of the inner and outer tubes during CNT pull-out leads to a small horizontal force (in $\boldsymbol{e}_2$ direction) and a twisting moment. Those are absent if the concentricity is not enforced. The FE simulations further show that it makes a difference where the displacements are prescribed. For the subsequent results, the displacements are applied at the center, and the forces are measured there. If the ends are used instead, then the forces and moments are offset slightly on the horizontal axis in Figs. 14 and 21.

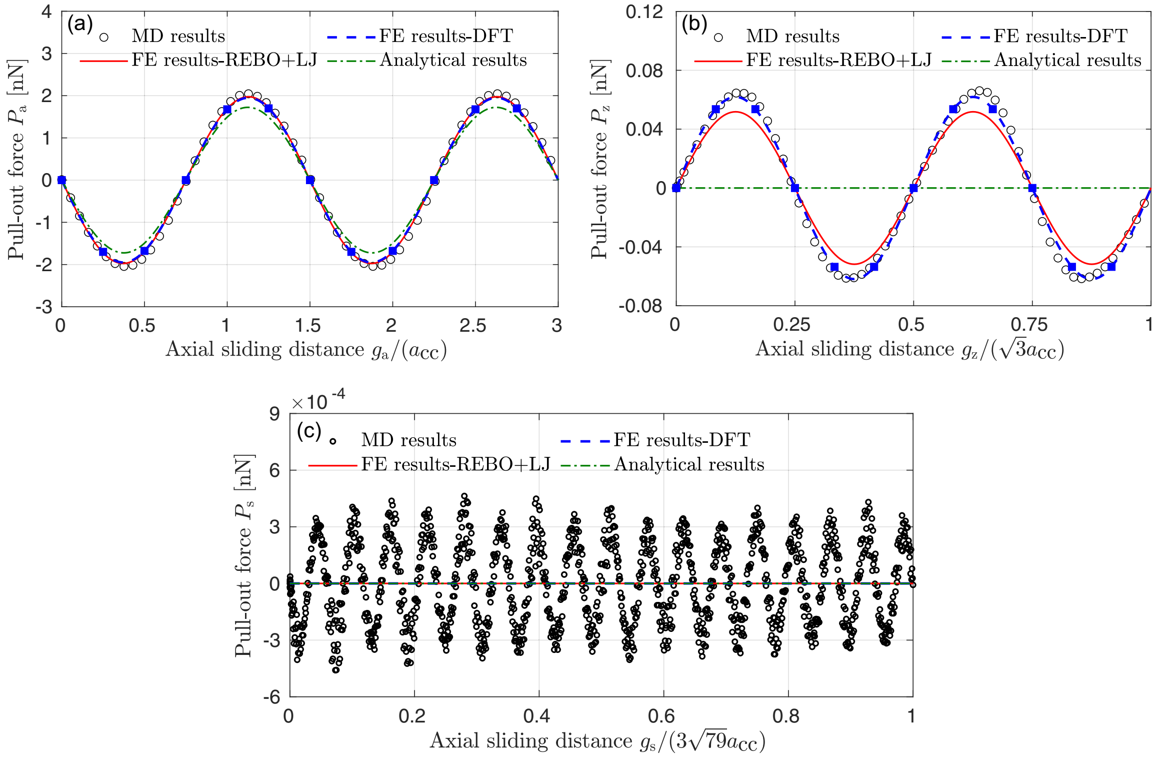

FIG. 14. Pull-out force for (a) Case 1, (b) Case 2, and (c) Case 3 in dependence of the axial sliding distance. The corresponding contact tractions for the 12 locations marked by blue squares in (a) and (b) are illustrated in Figs. 15–18.

B. CNT pull-out

Next, the pull-out results are presented and discussed. The FE results are compared to analytical results (derived in Appendix D) and MD results.

1. *General observations*

The length of the axial unit cell of each CNT is defined by its two chiral indices (n, m) and is given by $\ell = \sqrt{3}L_c/d_R$, where L_c is the circumference of the CNT and d_R is the greatest common divisor (GCD) of $2n + m$ and $2m + n$ [71]. This implies that the pull-out force has a periodicity equal to its unit cell length along the axial direction. For the three cases of CNTs considered here, the unit cell lengths are, respectively, $\ell_1 = 3a_{\rm cc} = 0.4191$ nm, $\ell_2 = \sqrt{3}a_{\rm cc} = 0.2420$ nm, and $\ell_3 = 3\sqrt{79}a_{\rm cc} = 3.7250$ nm.

The FE simulations are carried out using two sets of material properties: Determined from (1) DFT [80] and (2) MD using REBO+LJ potential (see Appendix B and Table VII for details). Further, the FE simulations based on the contact formulation of Sec. III assume that the neighboring CNT (outer or inner, respectively) is treated rigidly, while deformations are accounted for in the considered CNT itself. Still, the initial deformation of the neighboring CNT is accounted for by using the relaxed radii from Table III. Comparison plots of the pull-out forces determined from FE, MD, and analytical results are shown in Fig. 14. The periodicity obtained from these approaches agrees well with the theoretical predictions. Also, the amplitude agrees well for the FE and MD results. This is also seen in Table IV, which compares the absolute difference between the maximum pull-out force. The amplitude of the pull-out force, defined as $P_s^{\max} - P_s^{\min}$ during the sliding for Case 1 obtained from the MD simulations, is 4.091 nN. These amplitudes are 0.132 and 9.6486×10^{-4} nN, respectively, for Cases 2 and 3, which are ≈96.77% and ≈99.98% less than that for Case 1. Thus, the pull-out force amplitudes are sensitive to the chirality of the CNTs, with the maximum for zigzag and the minimum for chiral CNTs. While the relative differences between MD and FE results increase from Case 1 to 3, their absolute difference decreases, as seen in Table IV.

2. *Case 1: Pull-out of CNT(26,0) from within CNT(35,0)*

Figures 15 and 16 show the FE contact pressure and axial contact traction during pull-out for Case 1 using the DFT parameters. The contact forces vary in circumferential direction as a consequence of the circumferential interference noted in Sec. III. Only at $g_a = \ell_a/4$ and $g_a = 3\ell_a/4$ is the pressure uniform, while the axial traction is zero at $g_a = 0$ and $g_a = \ell_a/2$. As noted in Table III, the CNTs in Case 1 are in a state of attraction. As a consequence, there are circum-

TABLE IV. Absolute differences in the maximum pull-out force between MD and FE.

Case	$P_s^{\max}$(MD) − $P_s^{\max}$(FE-DFT) (nN)	$P_s^{\max}$(MD) − $P_s^{\max}$(FE-REBO+LJ) (nN)
1	95.0626×10^{-3}	70.9569×10^{-3}
2	4.6490×10^{-3}	14.7392×10^{-3}
3	0.4739×10^{-3}	0.4740×10^{-3}

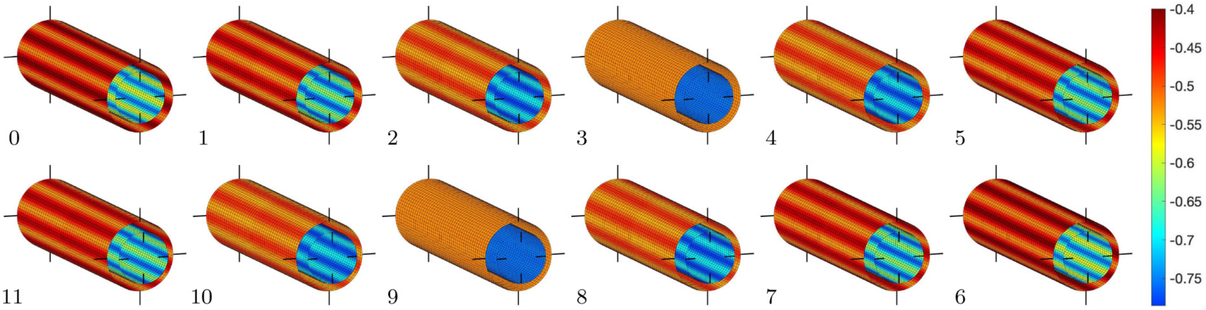

FIG. 15. Pull-out of CNT(26,0) from within CNT(35,0) (Case 1): Color plot of contact pressure p in GPa at $g_a \in [0,\ 1,\ 2, \dots,\ 11] \cdot \ell_a/12$ (clockwise, starting top left).

ferential stresses in the tubes, leading to the axial strains $\varepsilon_{\text{out}} = 3.616 \times 10^{-4}$ and $\varepsilon_{\text{in}} = -3.887 \times 10^{-4}$ in the initially relaxed configuration of the outer and inner tube, respectively. As seen in Fig. 14(a), the periodicity and amplitude of the pull-out force determined from the FE simulations using the DFT parameters agree well with those obtained from the MD simulations. There is no error in the period, while the amplitudes differ by ≈5% in relative and $\approx 95.0626 \times 10^{-3}$ nN in absolute terms. The FE results with the REBO+LJ parameters are even more accurate as Fig. 14(a) and Table IV show. The accuracy of the FE results can be further assessed by examining the difference of the pull-out forces acting on the inner and outer CNT. In theory, these forces should be in exact equilibrium. But due to the rigid master assumption made in Sec III, a slight difference can appear. Here this difference is below 2.82% compared to the average pull-out force shown in Fig. 14(a). This difference is very small and thus justifies the rigid master CNT assumption.

3. Case 2: Pull-out of CNT(15,15) from within CNT(20,20)

Figures 17 and 18 show the contact pressures and axial contact tractions for Case 2 determined from the FE simulations using the DFT parameters. Again, the contact tractions vary in circumferential direction during sliding. The axial traction is zero at $g_z = 0$ and $g_z = \ell_z/2$. The CNTs for this case are in a state of repulsion, which leads to positive contact pressures. As a consequence, the axial strain of the outer and inner CNT are $\varepsilon_{\text{out}} = -1.996 \times 10^{-4}$ and $\varepsilon_{\text{in}} = 2.189 \times 10^{-4}$, respectively, in the initially relaxed configuration. The maximum pull-out force from FE simulations compares well with that determined from MD simulations, with an absolute error of 4.6490×10^{-3} nN (see Table IV), which is much smaller than for Case 1. Relative errors, however, have increased as Fig. 14(b) shows. Also, the relative difference of the FE pull-out force on inner and outer CNT has increased, and is now below ≈18.42% compared to the average pull-out force shown in Fig. 14(b). The rigid master assumption thus introduces a significant inaccuracy in Case 2. Furthermore, the FE pull-out force based on the elasticity parameters computed from the REBO+LJ potential is significantly smaller than that based on the elasticity parameters computed from DFT.

4. Case 3: Pull-out of CNT(21,9) from within CNT(28,12)

Figures 19 and 20 show the contact pressures and axial tractions for Case 3 determined from FE using the DFT parameters. Again, the contact pressure and axial tractions vary circumferentially during axial sliding. Case 3 is in a state of attraction; therefore, there is adhesion between the tubes, leading to the axial strains $\varepsilon_{\text{out}} = 2.107 \times 10^{-4}$ and $\varepsilon_{\text{in}} = -1.982 \times 10^{-4}$ in the initially relaxed configuration for the outer and inner tube, respectively. The periodicity of the pull-out force determined from FE is $\ell_3 = 3\sqrt{79}a_{\text{cc}}$, which is exactly the same as that obtained from the MD and theoretical calculations [see Fig. 14(c) and Sec. VI B 1]. The maximum amplitude of the pull-out forces determined from MD and FE using DFT and REBO+LJ parameters are, respectively, 4.7×10^{-4}, 1.4×10^{-7}, and 8.4×10^{-8} nN. The maximum pull-out forces obtained from FE differ with respect to MD by 0.4739×10^{-3} and 0.4740×10^{-3} nN for the two material parameters considered, see Table IV. These small differences

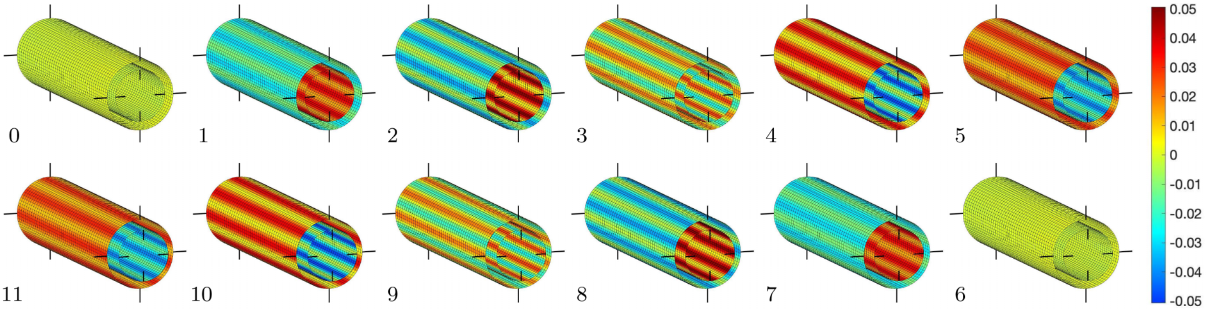

FIG. 16. Pull-out of CNT(26,0) from within CNT(35,0) (Case 1): Color plot of axial contact traction t^1 in GPa at $g_a \in [0,\ 1,\ 2, \dots,\ 11] \cdot \ell_a/12$ (clockwise, starting top left). The axial tractions in these 12 configurations sum up to the pull-out forces marked in Fig. 14(a).

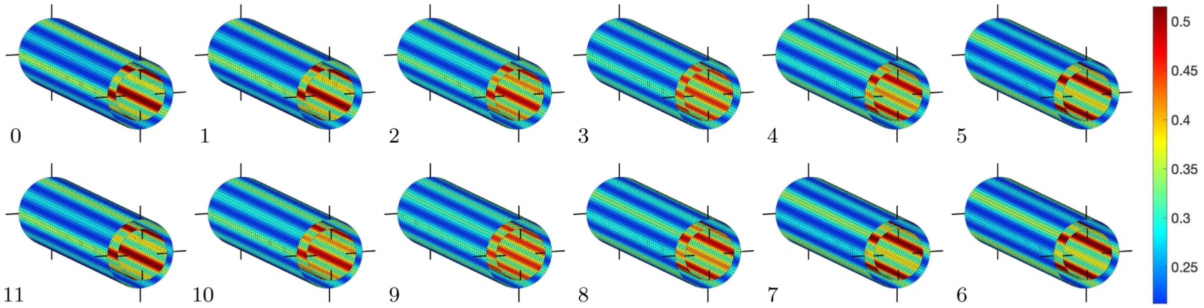

FIG. 17. Pull-out of CNT(15,15) from within CNT(20,20) (Case 2): Color plot of contact pressure p in GPa at $g_z \in [0,\ 1,\ 2, \ldots,\ 11] \cdot \ell_z/12$ (clockwise, starting top left).

can be attributed to several small discrepancies between MD and FE. One is the rigidity assumption of the contact master surface, which introduces the relative difference of $\approx 3.35 \times 10^{-4}$ compared to the maximum MD force, which seems insignificant. A second are the differences between the chosen continuum ansatz (2) and the MD data. But also those are very small as seen in Sec. IV C. A third are the boundary conditions: In the FE simulations, the rotation of the CNT about its axis is constrained, which is a displacement boundary condition. On the other hand, due to the limitation in LAMMPS, this boundary condition cannot be applied directly, and is mimicked by applying torsional springs to the circumferential atoms, which corresponds to a force boundary condition. As a result, the reaction torques during pull-out cause small rotational oscillations leading to fluctuations in the pull-out forces. The MD data plotted in Fig. 14 is filtered using a moving average approach with window/sample length 5, 20, and 100 for cases 1, 2 and 3, respectively. These fluctuations are minute for Case 1. However, at smaller pull-out forces, these fluctuations become much more significant, particularly for Case 3. Thus, the differences in the pull-out forces determined from FE and MD may be due to the rotational oscillations in the MD simulations.

5. *Pull-out summary*

For all three cases, the FE simulations predict pull-out behavior very similar to that of MD. The amplitudes are found to be sensitive to the continuum material properties used, as seen in Fig. 14 and Table IV. Those material parameters are based on decoupled membrane and bending models. In MD simulations, on the other hand, the bending stiffness of graphene is calculated by computing the potential energies of relaxed CNTs with respect to the ground-state potential energy of graphene. In such cases, the energy of relaxed CNTs is not just associated with the curvature of the CNTs but also the membrane strain energy.

In contrast to MD and FE simulations, the analytical results shown in Fig. 14 and derived in Appendix D are for rigid CNTs. Therefore, the differences in the pull-out forces determined from the FE/MD and analytical expression show the contribution of the elastic nature of CNTs. Case 1 is the only case where a pull-out force is generated independent of the CNT deformation (i.e., corresponding to the analytical result). In all other cases the pull-out force is a higher-order effect coming solely from the CNT deformation. This is seen through the analytical solution as it does not capture this higher-order effect.

C. CNT within CNT twisting

Finally, the twisting results are presented and discussed. As before, the FE results are compared to analytical results (derived in Appendix D) and MD results.

1. *Rotational symmetry*

Similar to the axial symmetry, the rotational symmetry of DWCNTs also depends on the chiral indices of each CNT. According to the elementary number theory, the inter-wall interaction energy due to inner CNT rotation and thus their re-

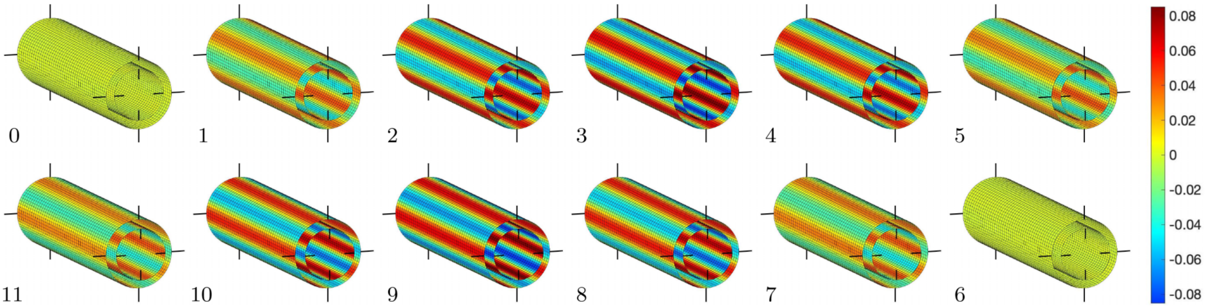

FIG. 18. Pull-out of CNT(15,15) from within CNT(20,20) (Case 2): Color plot of axial contact traction t_1 in [GPa] at $g_z \in [0,\ 1,\ 2, \ldots,\ 11] \cdot \ell_z/12$ (clockwise, starting top left).

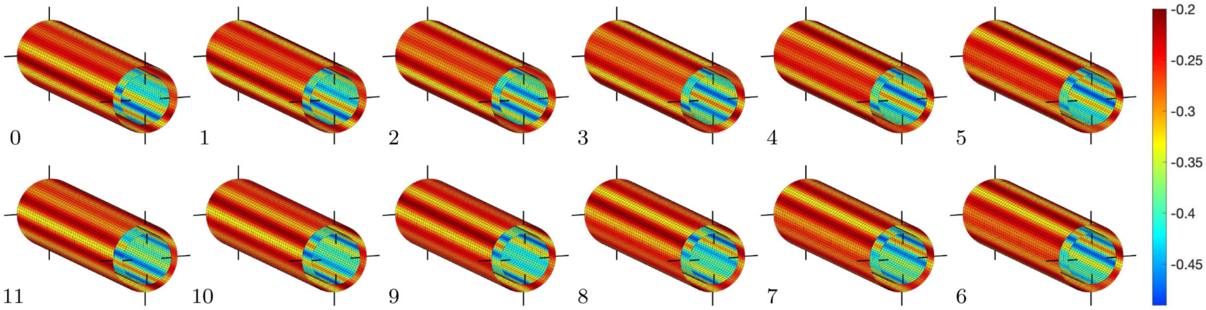

FIG. 19. Pull-out of CNT(21,9) from within CNT(28,12) (Case 3): Color plot of contact pressure p in GPa at $u = [0, 1, 2, \ldots, 11] \cdot \ell_3/200$ (clockwise, starting top left).

sisting torque has periodicity of GCD $(n_1, n_2)/(n_1 n_2) \times 360^\circ$, where the inner and outer CNTs have n_1-fold and n_2-fold symmetries, respectively [81]. For Case 1, the inner CNT thus has 26-fold rotational symmetry, while the outer one has 35. Therefore, the resisting torque must have a 0.3956° periodicity. Similarly, for Cases 2 and 3 the inner CNTs have 15- and 3-fold rotational symmetries, while outer ones have 20- and 4-fold, respectively. Therefore, the resisting torque in Cases 2 and 3 must have a rotational periodicity of 6° and 30°, respectively.

2. Twisting results

The comparison of the resisting torque as a function of the rotation angle of the inner CNT between FE, MD, and analytical expression is shown in Fig. 21. The FE and analytical torques are zero, while for MD, the amplitude of the torques, defined as $M_T^{\max} - M_T^{\min}$, are 1.7051×10^{-4}, 6.6415×10^{-3}, and 1.3077×10^{-3} nN nm for Cases 1, 2, and 3, respectively. As in the case of pull-out, the periodicity and amplitude of the resisting torques of CNT within CNT twisting depend on the chirality of the CNTs. The periodicity of the resisting torque determined from the MD simulations agrees well with the theoretical calculations. Figures 22–24 show the contact pressures and circumferential tractions during twisting for the three cases determined from the FE simulations using the DFT parameters. In all three cases, due to the circumferential interference the contact forces and pressures vary in circumferential direction.

3. Twisting summary

As seen in Fig. 21, the torques from FE and analytical integration vanish. The MD torques are nonzero, but they are much smaller than what could have been expected from the pull-out forces observed in Fig. 14: Multiplying the pull-out force amplitudes by the DWCNT radii gives 2.052 nN-nm, 0.102 nN-nm, and 0.035 nN-nm for the three cases, which is much higher than the torques observed for Cases 1 and 2. The reason for the difference between MD and FE torques is expected to lie in the insufficient MD boundary conditions and/or the approximate FE contact master surface treatment noted earlier. The analytical result are based on the assumption that all deformations are negligible. As a consequence, their interaction integrates to zero.

VII. CONCLUSION

This work proposes a new continuum contact model to describe the interlayer interactions of curved graphene sheets in continuum formulations such as the finite-element method. The interaction between two flat graphene layers shows nondissipative sliding behavior when the separation gap between the two layers is larger than 0.29 nm. Thus, the interaction energy can be modeled using a surface potential that is then calibrated for various separation gaps between the sheets. The

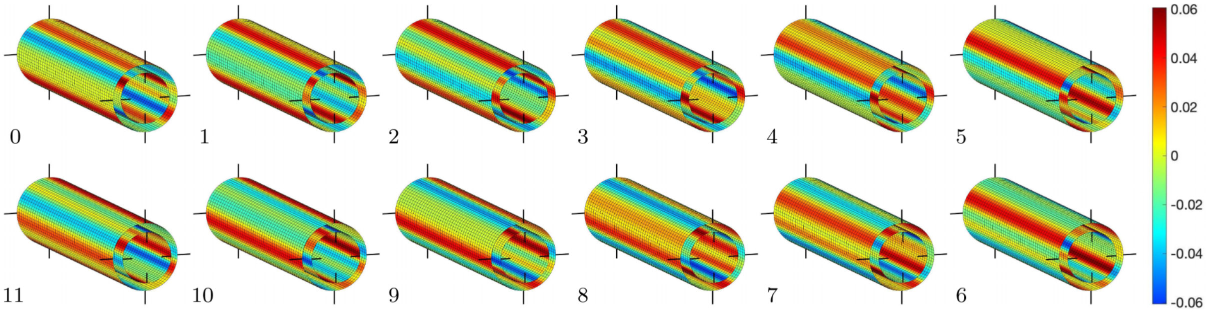

FIG. 20. Pull-out of CNT(21,9) from within CNT(28,12) (Case 3): Color plot of axial contact traction t^1 in GPa at $u = [0, 1, 2, \ldots, 11] \cdot \ell_3/200$ (clockwise, starting top left).

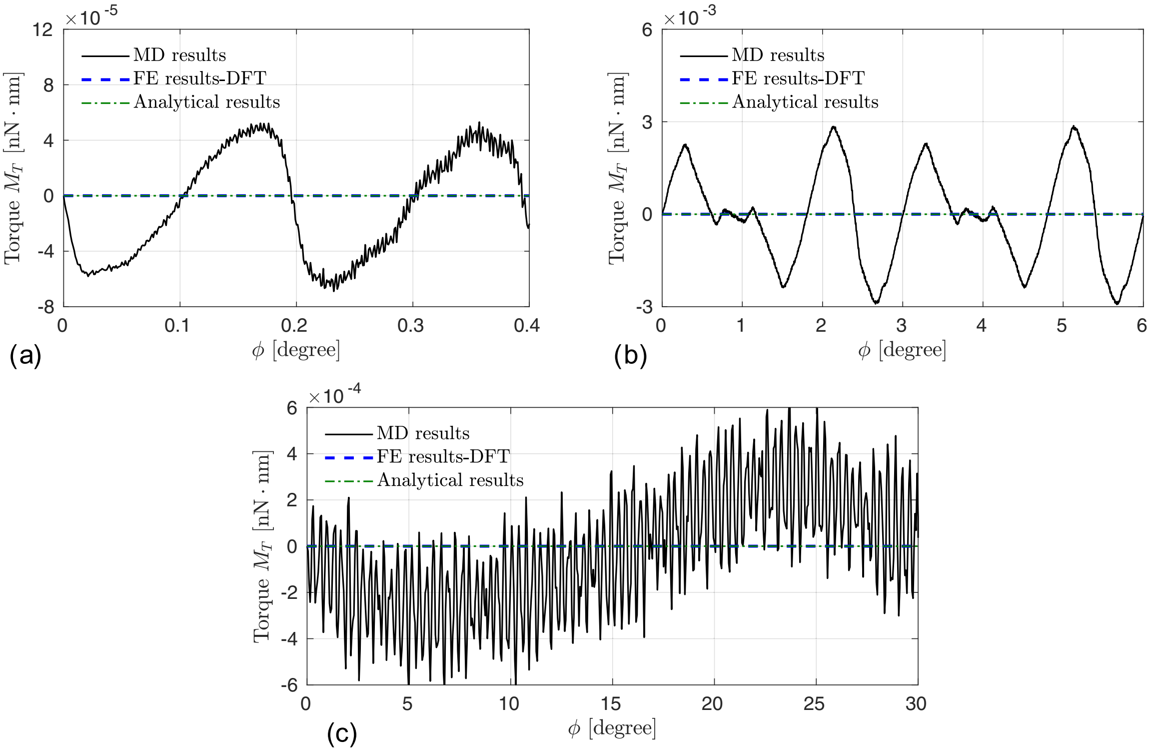

FIG. 21. CNT within CNT twisting: Variation of the resisting torque for (a) Case 1, (b) Case 2, and (c) Case 3 with rotation angle ϕ.

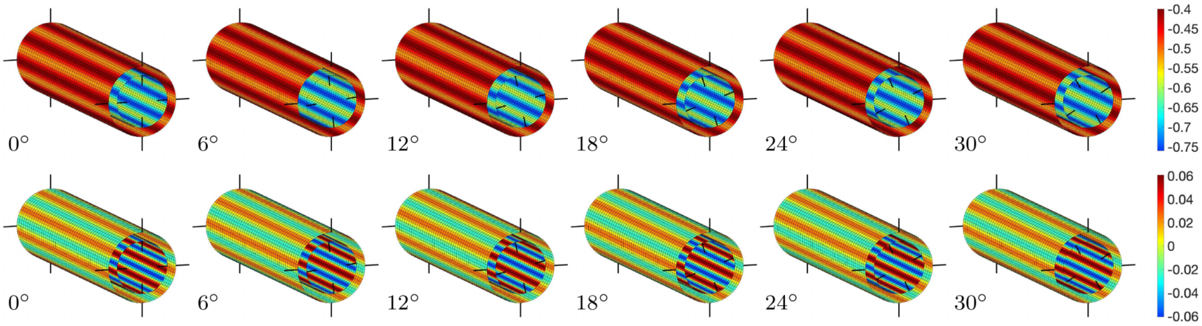

FIG. 22. Twisting CNT(26,0) inside CNT(35,0) (Case 1): Color plot of contact pressure p in GPa (top row) and circumferential traction t^2 in GPa (bottom row) at 0°, 6°, 12°, 18°, 24°, and 30° twist of the inner CNT, from left to right. The inner CNT is twisted counterclockwise. The pressure and traction patterns move counterclockwise on both CNTs, and they are faster than the twisting rate.

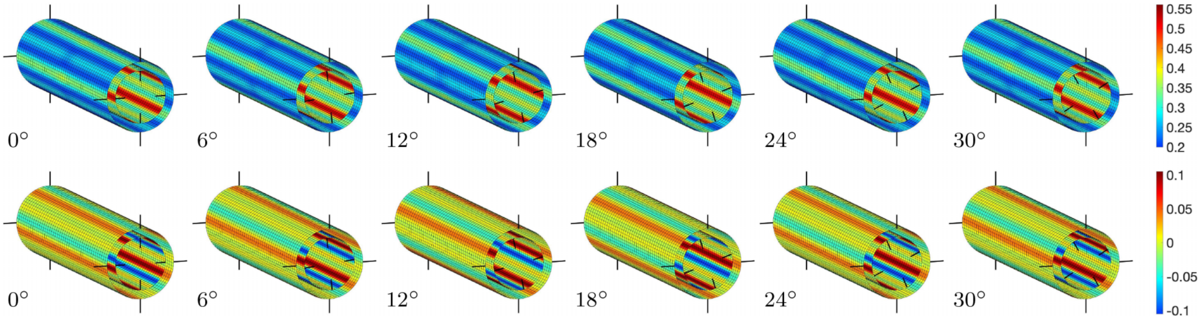

FIG. 23. Twisting CNT(15,15) inside CNT(20,20) (Case 2): Color plot of contact pressure p in GPa (top row) and circumferential traction t^2 in GPa (bottom row) at 0°, 6°, 12°, 18°, 24°, and 30° twist of the inner CNT, from left to right. The inner CNT is twisted counterclockwise. The pressure and traction patterns move counterclockwise on both CNTs, and they are faster than the twisting rate: three times faster on the outer CNT and four times faster on the inner CNT.

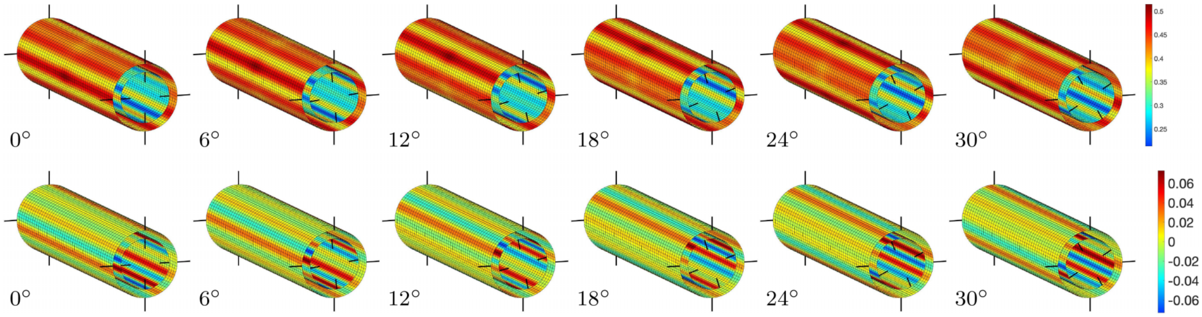

FIG. 24. Twisting CNT(21,9) inside CNT(28,12) (Case 3): Color plot of contact pressure p in GPa (top row) and circumferential traction t^2 in GPa (bottom row) at 0°, 6°, 12°, 18°, 24°, and 30° twist of the inner CNT, from left to right. The inner CNT is twisted counterclockwise. The pressure and traction patterns move counterclockwise on both CNTs, and they are faster than the twisting rate.

calibrated continuum model captures the sliding anisotropy of bilayer graphene for general sliding distances, both for the interaction potential and the resulting contact traction. The proposed continuum model is then implemented in a curvilinear finite-element shell formulation to study the interactions of DWCNTs. Zigzag CNTs, whose axis is along the armchair direction, show maximum resistance to sliding, while the minimum is for chiral CNTs. The periodicity of pull-out forces and torques also depends on the chirality of DWCNTs. The FE simulations capture these CNT pull-out and twisting interactions sufficiently well.

ACKNOWLEDGMENTS

Financial support from the German Research Foundation (DFG) through Grant No. SA1822/8-1 is gratefully acknowledged. The authors also thank Reza Ghaffari and Thang X. Duong for their support.

APPENDIX A: COMPARISON OF INTERLAYER INTERACTION POTENTIALS

Here we describe the interatomic potentials used and compare the calibration results of Sec. IV with those obtained from different interaction potentials available in the literature, such as the Kolmogorov and Crespi [34] and Lebedeva *et al.* [35] potentials.

The REBO potential is given by

$$E_{\mathrm{REBO}} = \sum_{I} \sum_{J=I+1} [E_R(r_{IJ}) + b_{IJ}\, E_A(r_{IJ})], \tag{A1}$$

where r_{IJ} is the distance between the pair of atoms I and J, and b_{IJ} is an empirical bond-order term. E_R and E_A are, respectively, the repulsive and attractive terms taken from Stuart *et al.* [59]. The LJ term is given by

$$E_{\mathrm{LJ}} = 4\epsilon_c \left[\left(\frac{\sigma_c}{r_{IJ}} \right)^{12} - \left(\frac{\sigma_c}{r_{IJ}} \right)^{6} \right], \tag{A2}$$

where $\sigma_c = 3.4$ Å and $\epsilon_c = 2.8437$ meV are the LJ parameters for carbon. In the REBO+LJ potential, the REBO part describes the short-range interactions, whereas the LJ part describes the nonbonded vdW interactions (see Stuart *et al.* [59] for details and the potential parameters). The KC potential is given by [34]

$$\begin{aligned} E_{\mathrm{KC}} &= e^{-\tilde{\lambda}(r_{IJ}-z_0)}[C + f(\rho_{IJ}) + f(\rho_{JI})] - A\left(\frac{z_0}{r_{IJ}}\right)^6, \\ \rho_{IJ}^2 &= r_{IJ}^2 - (\boldsymbol{n}_I \cdot \boldsymbol{r}_{IJ})^2, \\ \rho_{JI}^2 &= r_{IJ}^2 - (\boldsymbol{n}_J \cdot \boldsymbol{r}_{IJ})^2, \text{ and} \\ f(\rho) &= e^{-(\rho/\delta)^2} \sum_{n=0}^{2} C_{2n} (\rho/\delta)^{2n}, \end{aligned} \tag{A3}$$

where the vector $\boldsymbol{n}_k$ $(k = I, J)$ is normal to the sp^2 plane in the vicinity of atom k, and $z_0 = 3.33$ Å, $C_0 = 21.84$ meV, $C_2 = 12.06$ meV, $C_4 = 4.711$ meV, $C = 6.678 \times 10^{-4}$ meV, $\delta = 0.7718$ Å, $\tilde{\lambda} = 3.143$ Å^{-1}, and $A = 12.66$ meV are the potential constants, taken from Ouyang *et al.* [75].

The Lebedeva potential function is given by [35]

$$\begin{aligned} &E_{\mathrm{Lebedeva}} \\ &\quad = B\, e^{-\alpha(r_{IJ}-z_0)} + C(1 + D_1\, \rho_{IJ}^2 + D_2\, \rho_{IJ}^4) e^{-\tilde{\lambda}_1 \rho_{IJ}^2 - \tilde{\lambda}_2 (z_{IJ}^2 - z_0^2)} \\ &\qquad - A\left(\frac{z_0}{r_{IJ}}\right)^6, \end{aligned} \tag{A4}$$

where $A = 10.510$ meV, $B = 11.652$ meV, $C = 35.883$ meV, $z_0 = 3.34$ Å, $\alpha = 4.16$ Å^{-1}, $D_1 = -0.86232$ Å^{-2}, $D_2 = 0.1005$ Å^{-4}, $\tilde{\lambda}_1 = 0.487$ Å^{-2}, and $\tilde{\lambda}_2 = 0.46445$ Å^{-2} are the potential constants [35].

In the MD simulations, the interlayer interactions are now defined using these potentials. Figure 25 shows that their normal contact and tangential sliding behavior are qualitatively the same. Therefore, the same potential ansatz functions for Ψ_{flat}, $\bar{\Psi}_t$, Ψ_1, and Ψ_2 are used and the same procedure described in Sec. IV is followed to determine the constants in Eqs. (43) and (46). These values are listed in Table V.

TABLE V. Fitting constants of Eq. (43) and Eq. (46) for different interaction potentials.

Potential	p_{01} (nN/nm^2)	g_{01} (nm)	p_{02} (nN/nm^2)	g_{02} (nm)
LJ	5.8646	0.3376	4.404×10^6	1.875×10^{-2}
KC	5.6448	0.3410	3.306×10^4	3.140×10^{-2}
Lebedeva	4.9625	0.3460	3.985×10^4	3.160×10^{-2}

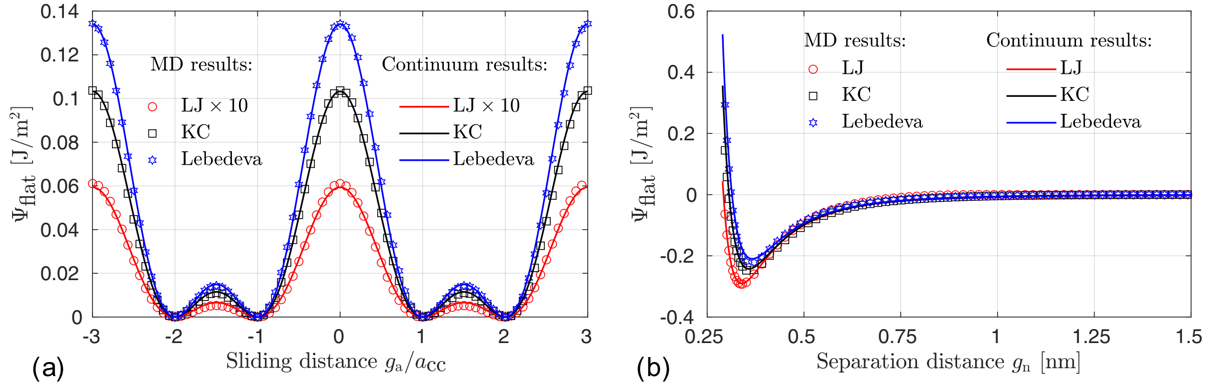

FIG. 25. Comparison of the interaction energy for (a) sliding along the armchair path at $g_n = 0.3366$ nm and (b) for $g_a = 0$ and $g_z = 0$ (AA stacking) as a function of separation distance g_n. For better comparability, the results in (a) are plotted relative to the global minimum and the LJ results are scaled by a factor of 10.

The potential relief characteristics, such as the relative energy between AA and AB stacking ($\Delta\Psi_{\rm flat}^{\rm AA}$), the relative energy between AB and SP stacking ($\Delta\Psi_{\rm flat}^{\rm SP}$), and equilibrium distances of different stackings are listed in Table VI. The separation distance is set to the equilibrium distance of the AB stacking. The potential relief characteristics obtained from the Lebedava potential agree better with the DFT data [35] than the other two interaction potentials. As noted already, the interaction behavior is qualitatively the same. Therefore, according to Eq. (54), the tangential tractions only differ by the factors $\Psi_2^{\rm KC}/\Psi_2^{\rm LJ}$ and $\Psi_2^{\rm Lebedeva}/\Psi_2^{\rm LJ}$ for the KC and Lebedeva interaction potentials, respectively.

APPENDIX B: ELASTIC CONSTANTS FOR GRAPHENE

Here we calculate the elastic properties of a single layer graphene sheet (SLGS). The SLGS is stretched along the armchair direction to calculate these elastic properties while applying constraints to the lateral edge atoms. The stress along the stretch direction (σ_{11}) and perpendicular to the stretch direction (σ_{22}) is shown in Fig. 26. Within the small strain regime, the SLGS behaves like an isotropic material [82], described by Hooke's law,

$$\sigma_{ij} = 2\,\mu\,\varepsilon_{ij} + \lambda\,\delta_{ij}\,\varepsilon_{kk}, \tag{B1}$$

where σ_{ij} and ε_{ij} are the stress and strain components, respectively, δ_{ij} is the Kronecker delta, and λ and μ are the Lamé constants. The 2D Young's modulus ($E_{\rm 2D}$) and Poisson's ratio (ν) are then determined through $\mu = E_{\rm 2D}/[2(1+\nu)]$ and $\lambda = 2\,\mu\,\nu/(1-\nu)$. The bending stiffness c_b is calculated by computing the potential energy of relaxed CNTs of different radii with respect to the ground-state graphene sheet [83]. The potential energies as a function of curvatures are fitted by quadratic functions. The bending stiffness is then obtained taking double derivatives with respect to the curvature.

The elastic properties determined from the REBO+LJ potential and DFT simulations available in the literature [80] are given in Table VII. The REBO+LJ potential underestimates the 2D Young's modulus and Poisson's ratio by ∼10.5% and ∼15.8% compared to DFT, respectively. On the other hand, it overestimates the bending stiffness by 46.3% compared to DFT.

APPENDIX C: CONTACT LINEARIZATION

For a rigid master surface, the linearization of contact traction $\boldsymbol{t}_s$ from Sec. III D is characterized by the increment

$$\Delta\boldsymbol{t}_s = \frac{\partial\boldsymbol{t}_s}{\partial\boldsymbol{x}_s}\Delta\boldsymbol{x}_s. \tag{C1}$$

Applying the product rule to Eq. (34) gives

$$\frac{\partial\boldsymbol{t}_s}{\partial\boldsymbol{x}_s} = \boldsymbol{n}_p\otimes\frac{\partial p}{\partial\boldsymbol{x}_s} + p\,\frac{\partial\boldsymbol{n}_p}{\partial\boldsymbol{x}_s} + \boldsymbol{a}_\gamma^p\otimes\frac{\partial t^\gamma}{\partial\boldsymbol{x}_s} + t^\gamma\,\frac{\partial\boldsymbol{a}_\gamma^p}{\partial\boldsymbol{x}_s}, \tag{C2}$$

where

$$\begin{aligned}\frac{\partial p}{\partial\boldsymbol{x}_s} &= \frac{\partial p}{\partial g_n}\frac{\partial g_n}{\partial\boldsymbol{x}_s} + \frac{\partial p}{\partial g_{\rm cc}^\delta}\frac{\partial g_{\rm cc}^\delta}{\partial\boldsymbol{x}_s},\\ \frac{\partial t^\gamma}{\partial\boldsymbol{x}_s} &= \frac{\partial t^\gamma}{\partial g_n}\frac{\partial g_n}{\partial\boldsymbol{x}_s} + \frac{\partial t^\gamma}{\partial g_{\rm cc}^\delta}\frac{\partial g_{\rm cc}^\delta}{\partial\boldsymbol{x}_s},\end{aligned} \tag{C3}$$

TABLE VI. Interaction energy of the AB stacking ($\Psi_{\rm flat}^{\rm AB}$), relative energies between AA and AB stacking ($\Delta\Psi_{\rm flat}^{\rm AA}$) and between SP and AB stacking ($\Delta\Psi_{\rm flat}^{\rm SP}$) at equilibrium separation distance of the AB stacking, and equilibrium distances (d_0) obtained from different interaction potentials. The DFT results are from Lebedeva *et al.* [35].

Potential	$\Psi_{\rm flat}^{\rm AB}$ (meV/atom)	$\Delta\Psi_{\rm flat}^{\rm AA}$ (meV/atom)	$\Delta\Psi_{\rm flat}^{\rm SP}$ (meV/atom)	$d_0^{\rm AA}$ (nm)	$d_0^{\rm AB}$ (nm)	$d_0^{\rm SP}$ (nm)
LJ	−45.60	1.00	0.095	0.3394	0.3366	0.3370
KC	−48.90	15.40	1.600	0.3580	0.3307	0.3343
Lebedeva	−47.20	19.90	2.100	0.3667	0.3326	0.3373
DFT	−50.60	19.50	2.070	—	0.3325	—

TABLE VII. Elastic properties of SLGS obtained from MD and DFT simulations.

Method/potential	λ (N/m)	μ (N/m)	E_{2D} (N/m)	ν	c_b (nN-nm)
REBO+LJ	48.27	131.42	304.89	0.16	0.354
DFT [80]	69.01	143.05	340.46	0.19	0.242

follow from the chain rule. From this, Eq. (27) and Eq. (31) then follows

$$\boldsymbol{n}_p \otimes \frac{\partial p}{\partial \boldsymbol{x}_s} = \frac{\partial p}{\partial g_n}\,\boldsymbol{n}_p \otimes \boldsymbol{n}_p + \frac{\partial p}{\partial g^\delta_{\mathrm{cc}}}\,Q_c^{\delta\mu}\,\boldsymbol{n}_p \otimes \boldsymbol{a}^p_\mu,$$
$$\boldsymbol{a}^p_\gamma \otimes \frac{\partial t^\gamma}{\partial \boldsymbol{x}_s} = \frac{\partial t^\gamma}{\partial g_n}\,\boldsymbol{a}^p_\gamma \otimes \boldsymbol{n}_p + \frac{\partial t^\gamma}{\partial g^\delta_{\mathrm{cc}}}\,Q_c^{\delta\mu}\,\boldsymbol{a}^p_\gamma \otimes \boldsymbol{a}^p_\mu. \qquad \text{(C4)}$$

Further,

$$\frac{\partial \boldsymbol{n}_p}{\partial \boldsymbol{x}_s} = \pm\frac{1}{R_m \pm g_n}\,\boldsymbol{a}^p_2 \otimes \boldsymbol{a}^p_2 \qquad \text{(C5)}$$

[72], and

$$\frac{\partial \boldsymbol{a}^p_1}{\partial \boldsymbol{x}_s} = \boldsymbol{0}, \qquad \frac{\partial \boldsymbol{a}^p_2}{\partial \boldsymbol{x}_s} = \mp\frac{1}{R_m \pm g_n}\,\boldsymbol{n}_p \otimes \boldsymbol{a}^p_2, \qquad \text{(C6)}$$

which follow from Eq. (21) and Eq. (30) and the chain rule

$$\frac{\partial \boldsymbol{a}^p_\alpha}{\partial \boldsymbol{x}_s} = \frac{\partial \boldsymbol{a}^p_\alpha}{\partial \xi^\gamma_p} \otimes \frac{\partial \xi^\gamma_p}{\partial \boldsymbol{x}_s}. \qquad \text{(C7)}$$

Equations (C5) and (C6) can also be written as

$$\frac{\partial \boldsymbol{n}_p}{\partial \boldsymbol{x}_s} = M^{\gamma\mu}\,\boldsymbol{a}^p_\gamma \otimes \boldsymbol{a}^p_\mu, \qquad \frac{\partial \boldsymbol{a}^p_\gamma}{\partial \boldsymbol{x}_s} = -M^\mu_\gamma\,\boldsymbol{n}_p \otimes \boldsymbol{a}^p_\mu, \qquad \text{(C8)}$$

with

$$[M^{\alpha\beta}] = -[M^\beta_\alpha] = \begin{bmatrix} 0 & 0 \\ 0 & \dfrac{\pm 1}{R_m \pm g_n} \end{bmatrix}. \qquad \text{(C9)}$$

Inserting Eq. (C4) and Eq. (C8) into Eq. (C2) then yields the gradient

$$\frac{\partial \boldsymbol{t}_s}{\partial \boldsymbol{x}_s} = \frac{\partial p}{\partial g_n}\,\boldsymbol{n}_p \otimes \boldsymbol{n}_p + \left(\frac{\partial p}{\partial g^\delta_{cc}}\,Q_c^{\delta\mu} - t^\gamma\,M^\mu_\gamma\right)\boldsymbol{n}_p \otimes \boldsymbol{a}^p_\mu,$$
$$+\frac{\partial t^\gamma}{\partial g_n}\,\boldsymbol{a}^p_\gamma \otimes \boldsymbol{n}_p + \left(\frac{\partial t^\gamma}{\partial g^\delta_{cc}}\,Q_c^{\delta\mu} + p\,M^{\gamma\mu}\right)\boldsymbol{a}^p_\gamma \otimes \boldsymbol{a}^p_\mu, \qquad \text{(C10)}$$

or

$$\frac{\partial \boldsymbol{t}_s}{\partial \boldsymbol{x}_s} = C_{nn}\,\boldsymbol{n}_p \otimes \boldsymbol{n}_p + C^\alpha_{na}\,\boldsymbol{n}_p \otimes \boldsymbol{a}^p_\alpha + C^\alpha_{an}\,\boldsymbol{a}^p_\alpha \otimes \boldsymbol{n}_p$$
$$+\,C^{\alpha\beta}_{aa}\,\boldsymbol{a}^p_\alpha \otimes \boldsymbol{a}^p_\beta, \qquad \text{(C11)}$$

with

$$\begin{aligned} C_{nn} &:= \frac{\partial p}{\partial g_n}, \\ C^\alpha_{na} &:= \frac{\partial p}{\partial g^\delta_{\mathrm{cc}}}\,Q_c^{\delta\alpha} - t^\gamma\,M^\alpha_\gamma, \\ C^\alpha_{an} &:= \frac{\partial t^\alpha}{\partial g_n}, \\ C^{\alpha\beta}_{aa} &:= \frac{\partial t^\alpha}{\partial g^\delta_{\mathrm{cc}}}\,Q_c^{\delta\beta} + p\,M^{\alpha\beta}. \end{aligned} \qquad \text{(C12)}$$

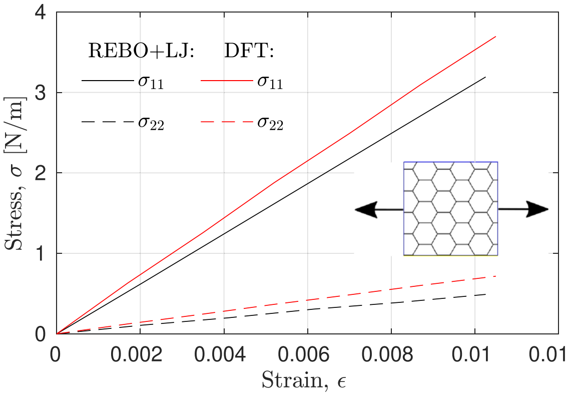

FIG. 26. Variation of the stress along the stretch direction, σ_{11}, and perpendicular to the stretch direction, σ_{22}, with the strain.

Equations (36)–(40) yield

$$\frac{\partial p}{\partial g_n} = \bar{S}\,(p'_1 + p'_2\,\bar{\Psi}_t), \qquad \frac{\partial p}{\partial g^\delta_{\mathrm{cc}}} = -\bar{S}\;p_2\,\bar{t}^c_\delta, \qquad \text{(C13)}$$

with $p'_i := \partial p_i/\partial g_n$, $i = 1, 2$, and

$$\begin{aligned} \frac{\partial t^\gamma}{\partial g_n} &= -\bar{S}\,p_2\,\bar{t}^c_\alpha\,Q_c^{\alpha\gamma}, \\ \frac{\partial t^\gamma}{\partial g^\delta_{\mathrm{cc}}} &= \bar{S}\,\Psi_2\,Q_{cT}^{\gamma\alpha}\,\frac{\partial \bar{t}^c_\alpha}{\partial g^\delta_{\mathrm{cc}}}. \end{aligned} \qquad \text{(C14)}$$

Since

$$\frac{\partial \bar{t}^c_\gamma}{\partial g^\delta_{\mathrm{cc}}} = -\frac{\partial^2 \bar{\Psi}_t}{\partial g^\gamma_{\mathrm{cc}}\,\partial g^\delta_{\mathrm{cc}}} = \frac{\partial \bar{t}^c_\delta}{\partial g^\gamma_{\mathrm{cc}}}, \qquad \text{(C15)}$$

Equations (C12)–(C14) result in

$$\begin{aligned} C_{nn} &= \bar{S}\,(p'_1 + p'_2\,\bar{\Psi}_t), \\ C^\alpha_{na} &= -\bar{S}\,p_2\,\bar{t}^c_\gamma\,Q_c^{\gamma\alpha}, \\ C^\alpha_{an} &= C^\alpha_{na}, \\ C^{\alpha\beta}_{aa} &= \bar{S}\,\Psi_2\,Q_{cT}^{\alpha\gamma}\,\frac{\partial \bar{t}^c_\gamma}{\partial g^\delta_{\mathrm{cc}}}\,Q_c^{\delta\beta} + p\,M^{\alpha\beta}. \end{aligned} \qquad \text{(C16)}$$

Since $C^\alpha_{an} = C^\alpha_{na}$ and $C^{\alpha\beta}_{aa} = C^{\beta\alpha}_{aa}$, the tangent is fully symmetric as it should be.

APPENDIX D: ANALYTICAL EXPRESSIONS FOR CNT PULL-OUT AND TWISTING

The axial pull-out force along $\boldsymbol{e}_1$ follows from integrating the traction t^1 over the slave CNT surface spanned by $\xi^1_{p0} \in [-L, L]/2$ and $\xi^2_{p0} \in [-\pi, \pi]R_s$, i.e.,

$$P = -\int_{-\frac{L}{2}}^{\frac{L}{2}}\int_{-\pi}^{\pi} t^1(g_a, g_z)\,R_s\,d\bar{\xi}^2_{p0}\,d\xi^1_{p0}. \qquad \text{(D1)}$$

The axial twisting moment (along $\boldsymbol{e}_1$) follows from integrating the moment $R_s\,t^2$ over the slave CNT surface, i.e.,

$$M_T = -\int_{-\frac{L}{2}}^{\frac{L}{2}}\int_{-\pi}^{\pi} t^2(g_a, g_z)\,R_s^2\,d\bar{\xi}^2_{p0}\,d\xi^1_{p0}. \qquad \text{(D2)}$$

The minus signs appear since P and M_T resists the tractions t^1 and t^2. According to Eqs. (36), (40), (42), (32), (24.2), and (30.2) the latter are given by

$$\begin{aligned} t^1 &= \bar{S}\,\Psi_2(\bar{t}_a\cos\theta - \bar{t}_z\sin\theta),\\ t^2 &= \bar{S}\,\Psi_2(\bar{t}_a\sin\theta + \bar{t}_z\cos\theta)\frac{R_m}{R_m \pm g_n}. \end{aligned} \tag{D3}$$

For rigid CNTs, the slave and master radii R_s and R_m are constant, and $R_m \pm g_n = R_s$. Expressions (D1)–(D3) can then be integrated analytically as is shown below. As noted in Sec. III B, integral type (D1) integrates equivalently over the inner CNT surface, the outer CNT surface, or the midsurface, since $\bar{S} = \bar{R}/R_s$, where $\bar{R}$ is the average radius. Only the sign of P differs on the outer and inner surface due to the sign difference of t^1 on those surfaces. Integral type (D2) integrates differently over both surfaces due to the factor R_m in front that is different on both surfaces. Equilibrium can therefore only be satisfied if M_T integrates to zero (for rigid CNTs).

1. Pull-out of CNT(26,0) from within CNT(35,0)

In this case the cylinder axis is aligned with the armchair direction ($\cos\theta = 1$, $\sin\theta = 0$), such that $t^1 = \bar{S}\,\Psi_2\,\bar{t}_a$ according to Eq. (D3.1). The initial gap is $G_n = R_{\text{out}} - R_{\text{in}} = 9\ell_z/(2\pi)$ and the length is denoted $L = L_a$. For rigid cylinders with $u := \xi^1_p - \xi^1_{p0}$, $\phi := \bar{\xi}^2_p - \bar{\xi}^2_{p0}$ and $\bar{\xi}^2_{p0} \in [-\pi, \pi]$, the axial and circumferential gaps now becomes

$$g_a = u, \quad g_z = \phi\,R_m \mp \frac{9\ell_z}{2\pi}\bar{\xi}^2_{p0} \tag{D4}$$

according to Eq. (18) and Eq. (19), respectively. The rear term of g_z lies in the interval $[-9, 9]\ell_z/2$. That is, g_z spans exactly nine periods of the interaction potential, irrespective of rotation angle ϕ. Therefore the rear term in Eq. (50.1) integrates to zero in Eq. (D1), while the front term leads to the analytical pull-out force (for all ϕ)

$$P_a(u) = -\bar{S}\,\Psi_2\,L_a\,\bar{R}\int_{-\pi}^{\pi}\bar{t}_a(g_a, g_z)\,d\bar{\xi}^2_{p0} = -P_{\max}\,\sin\frac{4\pi\,u}{\ell_a}, \tag{D5}$$

with the amplitude

$$P_{\max} = \frac{8\pi^2}{\ell_a}\,\Psi_2\,L_a\,\bar{R}. \tag{D6}$$

For $2\pi\bar{R} = 30.5\ell_z$, $\ell_z = \sqrt{3}a_{\text{cc}}$, and $L_a = 24\ell_a$ follows $P_{\max} = 2928\sqrt{3}\pi\,\Psi_2\,a_{\text{cc}}$. The value $a_{\text{cc}} = 0.1397$ nm then gives $G_n = 0.3466$ nm and $\Psi_2 = 7.7435 \times 10^{-4}$ nN/nm and $P_{\max} = 1.7235$ nN, which is the result shown in Fig. 14(a).

2. Pull-out of CNT(15,15) from within CNT(20,20)

In this case the cylinder axis is aligned with the zigzag direction ($\cos\theta = 0$, $\sin\theta = 1$), such that $t^1 = -\bar{S}\,\Psi_2\,\bar{t}_z$ according to Eq. (D3.1). The initial gap is $G_n = R_{\text{out}} - R_{\text{in}} = 5\ell_a/(2\pi)$ and the length is denoted $L = L_z$. For rigid cylinders, $\xi^1_p - \xi^1_{p0}$ corresponds to their relative axial motion u, while $\bar{\xi}^2_p - \bar{\xi}^2_{p0}$ corresponds to their relative rotation angle ϕ. Both are constant across the surface. Further, $\bar{\xi}^2_{p0} \in [-\pi, \pi]$. The axial and circumferential gaps thus become

$$g_z = u, \quad g_a = \phi\,R_m \mp \frac{5\ell_a}{2\pi}\bar{\xi}^2_{p0} \tag{D7}$$

according to Eq. (18) and Eq. (19), respectively. The rear term of g_a lies in the interval $[-5, 5]\ell_a/2$. That is, g_a spans exactly five periods of the interaction potential, irrespective of ϕ. Therefore the analytical pull-out force

$$P_z(u, \phi) = \Psi_2\,L_z\,\bar{R}\int_{-\pi}^{\pi}\bar{t}_z(g_a, g_z)\,d\bar{\xi}^2_{p0} \tag{D8}$$

from Eq. (D1) integrates to zero for all u and ϕ according to Eq. (50.2).

3. Pull-out of CNT(21,9) from within CNT(28,12)

In this case $\cos\theta = 17/(2\bar{c})$ and $\sin\theta = 3\sqrt{3}/(2\bar{c})$, with $\bar{c} := \sqrt{79}$, such that

$$t^1 = \frac{\bar{S}\,\Psi_2}{2\bar{c}}(17\,\bar{t}_a - 3\sqrt{3}\,\bar{t}_z), \tag{D9}$$

according to Eq. (D3.1). Inserting Eq. (50) then leads to

$$t^1 = \frac{2\pi\,\bar{S}\,\Psi_2}{\ell_u}[17\sin 2\hat{g}_a + 13\sin(\hat{g}_a - \hat{g}_z) + 4\sin(\hat{g}_a + \hat{g}_z)], \tag{D10}$$

where

$$\begin{aligned} \hat{g}_a &:= \frac{2\pi\,g_a}{\ell_a} = 17\pi\frac{u}{\ell_u} + \frac{3\pi\,R_m}{\ell_\phi}\phi \mp \frac{3}{2}\bar{\xi}^2_{p0},\\ \hat{g}_z &:= \frac{2\pi\,g_z}{\ell_z} = -9\pi\frac{u}{\ell_u} + \frac{17\pi\,R_m}{\ell_\phi}\phi \mp \frac{17}{2}\bar{\xi}^2_{p0} \end{aligned} \tag{D11}$$

follows from Eqs. (22), (18), and (19) and $G_n = \sqrt{3}\,\bar{c}\,a_{\text{cc}}/(2\pi)$ with $u := \xi^1_p - \xi^1_{p0}$, $\phi := \bar{\xi}^2_p - \bar{\xi}^2_{p0}$ and $\ell_u := \bar{c}\,\ell_a$, $\ell_\phi := \bar{c}\,\ell_z$. The front terms in Eq. (D11) do not change the fact that the three sine-terms in Eq. (D10) contain exactly 3, 7, and 10 full periods within $\bar{\xi}^2_{p0} \in [-\pi, \pi]$, respectively. Integral Eq. (D1) therefore vanishes, and the pull-out force becomes zero for all u and ϕ.

4. Twisting CNT(26,0) inside CNT(35,0)

In this case the cylinder axis is aligned with the armchair direction ($\cos\theta = 1$, $\sin\theta = 0$). The circumferential traction on the slave surface is therefore $t^2 = \bar{S}\,\Psi_2\,\bar{t}_z\,R_m/R_s$ according to Eq. (D3.2). As noted in Sec. D 1, the initial gap is $G_n = 9\ell_z/(2\pi)$ such that g_z spans exactly 9 periods of the interaction potential, see Eq. (D4). Therefore the analytical twisting moment

$$M_T(\phi, u) = -\Psi_2\,L_z\,\bar{R}\,R_m\int_{-\pi}^{\pi}\bar{t}_z(g_a, g_z)\,d\bar{\xi}^2_p \tag{D12}$$

from Eq. (D2) integrates to zero for all ϕ and u according to Eq. (50.2).

5. Twisting CNT(15,15) inside CNT(20,20)

In this case the cylinder axis is aligned with the zigzag direction ($\cos\theta = 0$, $\sin\theta = 1$). The circumferential traction on the slave surface is therefore $t^2 = \bar{S}\,\Psi_2\,\bar{t}_a\,R_m/R_s$, with $\bar{S} = \bar{R}/R_s$, according to Eq. (D3.2). As noted in Sec. D 2, the initial gap is $G_n = 5\ell_a/(2\pi)$ such that g_a spans exactly five periods of the interaction potential, see Eq. (D7). Therefore the analytical twisting moment

$$M_T(\phi, u) = -\Psi_2\, L_z\, \bar{R}\, R_m \int_{-\pi}^{\pi} \bar{t}_a(g_a, g_z)\, d\bar{\xi}_p^{\,2} \tag{D13}$$

from Eq. (D2) integrates to zero for all ϕ and u according to Eq. (50.1).

6. Twisting CNT(21,9) inside CNT(28,12)

In this case $\cos\theta = 17/(2\bar{c})$ and $\sin\theta = 3\sqrt{3}/(2\bar{c})$, $\bar{c} = \sqrt{79}$, such that

$$t^2 = \frac{\bar{S}\,\Psi_2\, R_m}{2\bar{c}\, R_s}(3\sqrt{3}\,\bar{t}_a + 17\,\bar{t}_z), \tag{D14}$$

according to Eq. (D3.2). Inserting Eq. (50) then leads to

$$t^2 = \frac{2\pi\, \bar{S}\,\Psi_2\, R_m}{\ell_\phi\, R_s}[3\sin 2\hat{g}_a - 7\sin(\hat{g}_a - \hat{g}_z) + 10\sin(\hat{g}_a + \hat{g}_z)], \tag{D15}$$

with $\hat{g}_a$ and $\hat{g}_z$ given in Eq. (D11). From Eq. (D11) again follows that the three sine-terms in Eq. (D15) contain exactly 3, 7, and 10 full periods within $\bar{\xi}_{p0}^{\,2} \in [-\pi, \pi]$, respectively. Integral Eq. (D2) therefore vanishes, and the twisting moment again becomes zero for all ϕ and u.

[1] K. Novoselov, A. Geim, S. Morozov, D. Jiang, Y. Zhang, and S. Dubonos *et al.*, Electric field effect in atomically thin carbon films, Science **306**, 666 (2004).

[2] G. S. Verhoeven, M. Dienwiebel, and J. W. M. Frenken, Model calculations of superlubricity of graphite, Phys. Rev. B **70**, 165418 (2004).

[3] Q. Zheng, B. Jiang, S. Liu, Y. Weng, L. Lu, Q. Xue, J. Zhu, Q. Jiang, S. Wang, and L. Peng, Self-retracting motion of graphite microflakes, Phys. Rev. Lett. **100**, 067205 (2008).

[4] D. Berman, A. Erdemir, and A. V. Sumant, Graphene: A new emerging lubricant, Mater. Today **17**, 31 (2014).

[5] M. Dienwiebel, G. S. Verhoeven, N. Pradeep, J. W. M. Frenken, J. A. Heimberg, and H. W. Zandbergen, Superlubricity of graphite, Phys. Rev. Lett. **92**, 126101 (2004).

[6] X. Feng, S. Kwon, J. Y. Park, and M. Salmeron, Superlubric sliding of graphene nanoflakes on graphene, ACS Nano **7**, 1718 (2013).

[7] Y. Cao, V. Fatemi, S. Fang, K. Watanabe, T. Taniguchi, E. Kaxiras, and P. Jarillo-Herrero, Unconventional superconductivity in magic-angle graphene superlattices, Nature (London) **556**, 43 (2018).

[8] C. Shen, Y. Chu, Q. Wu, N. Li, S. Wang, Y. Zhao, J. Tang, J. Liu, J. Tian, and K. Watanabe *et al.*, Correlated states in twisted double bilayer graphene, Nat. Phys. **16**, 520 (2020).

[9] J. S. Bunch, A. M. van der Zande, S. S. Verbridge, I. W. Frank, D. M. Tanenbaum, J. M. Parpia, H. G. Craighead, and P. L. McEuen, Electromechanical resonators from graphene sheets, Science **315**, 490 (2007).

[10] S. Bae, H. Kim, Y. Lee, X. Xu, J.-S. Park, Y. Zheng, J. Balakrishnan, T. Lei, H. Ri Kim, Y. I. Song *et al.*, Roll-to-roll production of 30-inch graphene films for transparent electrodes, Nat. Nanotechnol. **5**, 574 (2010).

[11] Y. Liu, N. O. Weiss, X. Duan, H.-C. Cheng, Y. Huang, and X. Duan, Van der Waals heterostructures and devices, Nat. Rev. Mater. **1**, 16042 (2016).

[12] M. Dienwiebel, N. Pradeep, G. S. Verhoeven, H. W. Zandbergen, and J. W. Frenken, Model experiments of superlubricity of graphite, Surf. Sci. **576**, 197 (2005).

[13] M. Reguzzoni, A. Fasolino, E. Molinari, and M. C. Righi, Potential energy surface for graphene on graphene: *Ab initio* derivation, analytical description, and microscopic interpretation, Phys. Rev. B **86**, 245434 (2012).

[14] J. M. B. Lopes dos Santos, N. M. R. Peres, and A. H. Castro Neto, Continuum model of the twisted graphene bilayer, Phys. Rev. B **86**, 155449 (2012).

[15] Z. Liu, The diversity of friction behavior between bi-layer graphenes, Nanotechnology **25**, 075703 (2014).

[16] H. Kumar, L. Dong, and V. B. Shenoy, Limits of coherency and strain transfer in flexible 2d van der waals heterostructures: Formation of strain solitons and interlayer debonding, Sci. Rep. **6**, 1 (2016).

[17] S. Wang, Y. Chen, Y. Ma, Z. Wang, and J. Zhang, Size effect on interlayer shear between graphene sheets, J. Appl. Phys. **122**, 074301 (2017).

[18] Z. Xue, G. Chen, C. Wang, and R. Huang, Peeling and sliding of graphene nanoribbons with periodic van der Waals interactions, J. Mech. Phys. Solids **158**, 104698 (2022).

[19] Y. Guo, W. Guo, and C. Chen, Modifying atomic-scale friction between two graphene sheets: A molecular-force-field study, Phys. Rev. B **76**, 155429 (2007).

[20] L. Xu, T.-B. Ma, Y.-Z. Hu, and H. Wang, Vanishing stick–slip friction in few-layer graphenes: The thickness effect, Nanotechnology **22**, 285708 (2011).

[21] A. M. Popov, I. V. Lebedeva, A. A. Knizhnik, Y. E. Lozovik, and B. V. Potapkin, Molecular dynamics simulation of the self-retracting motion of a graphene flake, Phys. Rev. B **84**, 245437 (2011).

[22] H. Zhang, Z. Guo, H. Gao, and T. Chang, Stiffness-dependent interlayer friction of graphene, Carbon **94**, 60 (2015).

[23] G. Wang, Z. Dai, Y. Wang, P. H. Tan, L. Liu, Z. Xu, Y. Wei, R. Huang, and Z. Zhang, Measuring interlayer shear stress in bilayer graphene, Phys. Rev. Lett. **119**, 036101 (2017).

[24] H. Li and W. K. Kim, A comparison study between the Lennard-Jones and DRIP potentials for friction of graphene layers, Comput. Mater. Sci. **180**, 109723 (2020).

[25] F. Afsharirad, S. Mousanezhad, H. Biglari, and O. Rahmani, Molecular dynamics of axial interwall van der Waals force and mechanical vibration of double-walled carbon nanotubes, Mater. Today Commun. **28**, 102708 (2021).

[26] E. J. Mele, Commensuration and interlayer coherence in twisted bilayer graphene, Phys. Rev. B **81**, 161405(R) (2010).

[27] M. Koshino and N. N. T. Nam, Effective continuum model for relaxed twisted bilayer graphene and moiré electron-phonon interaction, Phys. Rev. B **101**, 195425 (2020).

[28] G. A. Tomlinson, A molecular theory of friction, Lond. Edinb. Dubl. Philos. Mag. J. Sci. **7**, 905 (1929).

[29] H. L. Cox, The elasticity and strength of paper and other fibrous materials, Br. J. Appl. Phys. **3**, 72 (1952).

[30] J. Sun, Y. Zhang, Z. Lu, Q. Li, Q. Xue, S. Du, J. Pu, and L. Wang, Superlubricity enabled by pressure-induced friction collapse, J. Phys. Chem. Lett. **9**, 2554 (2018).

[31] M. Arroyo and T. Belytschko, Finite crystal elasticity of carbon nanotubes based on the exponential Cauchy-Born rule, Phys. Rev. B **69**, 115415 (2004).

[32] M. Arroyo and T. Belytschko, Finite element methods for the non-linear mechanics of crystalline sheets and nanotubes, Int. J. Numer. Methods Eng. **59**, 419 (2004).

[33] M. Arroyo and T. Belytschko, Continuum mechanics modeling and simulation of carbon nanotubes, Meccanica **40**, 455 (2005).

[34] A. N. Kolmogorov and V. H. Crespi, Registry-dependent interlayer potential for graphitic systems, Phys. Rev. B **71**, 235415 (2005).

[35] I. V. Lebedeva, A. A. Knizhnik, A. M. Popov, Y. E. Lozovik, and B. V. Potapkin, Interlayer interaction and relative vibrations of bilayer graphene, Phys. Chem. Chem. Phys. **13**, 5687 (2011).

[36] J.-W. Jiang and H. S. Park, A Gaussian treatment for the friction issue of Lennard-Jones potential in layered materials: Application to friction between graphene, MoS_2, and black phosphorus, J. Appl. Phys. **117**, 124304 (2015).

[37] M. Wen, S. Carr, S. Fang, E. Kaxiras, and E. B. Tadmor, Dihedral-angle-corrected registry-dependent interlayer potential for multilayer graphene structures, Phys. Rev. B **98**, 235404 (2018).

[38] I. Leven, T. Maaravi, I. Azuri, L. Kronik, and O. Hod, Interlayer potential for graphene/h-bn heterostructures, J. Chem. Theory Comput. **12**, 2896 (2016).

[39] T. Maaravi, I. Leven, I. Azuri, L. Kronik, and O. Hod, Interlayer potential for homogeneous graphene and hexagonal boron nitride systems: Reparametrization for many-body dispersion effects, J. Phys. Chem. C **121**, 22826 (2017).

[40] W. Ouyang, I. Azuri, D. Mandelli, A. Tkatchenko, L. Kronik, M. Urbakh, and O. Hod, Mechanical and tribological properties of layered materials under high pressure: Assessing the importance of many-body dispersion effects, J. Chem. Theory Comput. **16**, 666 (2020).

[41] A. Zmitrowicz, A theoretical model of anisotropic dry friction, Wear **73**, 9 (1981).

[42] A. Zmitrowicz, Mathematical descriptions of anisotropic friction, Int. J. Solids Struct. **25**, 837 (1989).

[43] A. Zmitrowicz, A constitutive modelling of centrosymmetric and non-centrosymmetric anisotropic friction, Int. J. Solids Struct. **29**, 3025 (1992).

[44] T. A. Laursen, *Computational Contact and Impact Mechanics: Fundamentals of Modeling Interfacial Phenomena in Nonlinear Finite Element Analysis* (Springer, Berlin, 2002).

[45] P. Wriggers, *Computational Contact Mechanics*, 2nd ed. (Springer, Berlin, 2006).

[46] J. K. Park and B. M. Kwak, Three-dimensional frictional contact analysis using the homotopy method, J. Appl. Mech. **61**, 703 (1994).

[47] R. Buczkowski and M. Kleiber, Elasto-plastic interface model for 3D-frictional orthotropic contact problems, Int. J. Numer. Methods Eng. **40**, 599 (1997).

[48] R. E. Jones and P. Papadopoulos, Simulating anisotropic frictional response using smoothly interpolated traction fields, Comput. Methods Appl. Mech. Eng. **195**, 588 (2006).

[49] A. Konyukhov and K. Schweizerhof, Covariant description of contact interfaces considering anisotropy for adhesion and friction: Part 1. Formulation and analysis of the computational model, Comput. Methods Appl. Mech. Eng. **196**, 103 (2006).

[50] A. Konyukhov and K. Schweizerhof, Covariant description of contact interfaces considering anisotropy for adhesion and friction: Part 2. Linearization, finite element implementation and numerical analysis of the model, Comput. Methods Appl. Mech. Eng. **196**, 289 (2006).

[51] L. Rodríguez-Tembleque and R. Abascal, Fast FE–BEM algorithms for orthotropic frictional contact, Int. J. Numer. Methods Eng. **94**, 687 (2013).

[52] I. Temizer, Computational homogenization of soft matter friction: Isogeometric framework and elastic boundary layers, Int. J. Numer. Methods Eng. **100**, 953 (2014).

[53] L. Rodríguez-Tembleque, R. Abascal, and M. H. Aliabadi, Anisotropic wear framework for 3d contact and rolling problems, Comput. Methods Appl. Mech. Eng. **241-244**, 1 (2012).

[54] S. Stupkiewicz, M. J. Lewandowski, and J. Lengiewicz, Micromechanical analysis of friction anisotropy in rough elastic contacts, Int. J. Solids Struct. **51**, 3931 (2014).

[55] R. A. Sauer, A frictional sliding algorithm for liquid droplets, Comput. Mech. **58**, 937 (2016).

[56] J. C. Mergel, R. Sahli, J. Scheibert, and R. A. Sauer, Continuum contact models for coupled adhesion and friction, J. Adhes. **95**, 1101 (2019).

[57] J. C. Mergel, J. Scheibert, and R. A. Sauer, Contact with coupled adhesion and friction: Computational framework, applications, and new insights, J. Mech. Phys. Solids **146**, 104194 (2021).

[58] L. Hu, Y. Cong, C. Renaud, and Z.-Q. Feng, A bi-potential contact formulation of orthotropic adhesion between soft bodies, Comput. Mech. **69**, 931 (2022).

[59] S. Stuart, A. Tutein, and J. Harrison, A reactive potential for hydrocarbons with intermolecular interactions, J. Chem. Phys. **112**, 6472 (2000).

[60] J. E. Jones, On the determination of molecular fields. II. from the equation of state of a gas, Proc. R. Soc. A **106**, 463 (1924).

[61] E. Polak and G. Ribiere, Note sur la convergence de méthodes de directions conjuguées, ESAIM: Math. Model. Num. **3**, 35 (1969).

[62] D. Evans and B. Holian, The Nose–Hoover thermostat, J. Chem. Phys. **83**, 4069 (1985).

[63] A. Mokhalingam, R. Ghaffari, R. A. Sauer, and S. S. Gupta, Comparing quantum, molecular and continuum models for graphene at large deformations, Carbon **159**, 478 (2020).

[64] W. C. Swope, H. C. Andersen, P. H. Berens, and K. R. Wilson, A computer simulation method for the calculation of equilibrium constants for the formation of physical clusters of molecules: Application to small water clusters, J. Chem. Phys. **76**, 637 (1982).

[65] S. Plimpton, Fast parallel algorithms for short-range molecular dynamics, J. Comput. Phys. **117**, 1 (1995).

[66] I. V. Lebedeva, A. A. Knizhnik, A. M. Popov, O. V. Ershova, Y. E. Lozovik, and B. V. Potapkin, Fast diffusion of a graphene flake on a graphene layer, Phys. Rev. B **82**, 155460 (2010).

[67] I. V. Lebedeva, A. A. Knizhnik, A. M. Popov, O. V. Ershova, Y. E. Lozovik, and B. V. Potapkin, Diffusion and drift of graphene flake on graphite surface, J. Chem. Phys. **134**, 104505 (2011).

[68] R. A. Sauer and P. Wriggers, Formulation and analysis of a 3D finite element implementation for adhesive contact at the nanoscale, Comput. Methods Appl. Mech. Eng. **198**, 3871 (2009).

[69] Y. Basar and Y. Ding, Finite-element analysis of hyperelastic thin shells with large strains, Comput. Mech. **18**, 200 (1996).

[70] R. A. Arciniega and J. N. Reddy, Tensor-based finite element formulation for geometrically nonlinear analysis of shell structures, AIAA J. **43**, 2024 (2005).

[71] M. Dresselhaus, G. Dresselhaus, and R. Saito, Physics of carbon nanotubes, Carbon **33**, 883 (1995).

[72] R. A. Sauer and L. De Lorenzis, A computational contact formulation based on surface potentials, Comput. Methods Appl. Mech. Eng. **253**, 369 (2013).

[73] L. A. Girifalco, M. Hodak, and R. S. Lee, Carbon nanotubes, buckyballs, ropes, and a universal graphitic potential, Phys. Rev. B **62**, 13104 (2000).

[74] V. Morovati, Z. Xue, K. M. Liechti, and R. Huang, Interlayer coupling and strain localization in small-twist-angle graphene flakes, Extreme Mech. Lett. **55**, 101829 (2022).

[75] W. Ouyang, D. Mandelli, M. Urbakh, and O. Hod, Nanoserpents: Graphene nanoribbon motion on two-dimensional hexagonal materials, Nano Lett. **18**, 6009 (2018).

[76] R. A. Sauer, An atomic interaction based continuum model for computational multiscale contact mechanics, Ph.D. thesis, University of California, Berkeley (2006).

[77] T. X. Duong, F. Roohbakhshan, and R. A. Sauer, A new rotation-free isogeometric thin shell formulation and a corresponding continuity constraint for patch boundaries, Comput. Methods Appl. Mech. Eng. **316**, 43 (2017).

[78] R. Ghaffari, T. X. Duong, and R. A. Sauer, A new shell formulation for graphene structures based on existing *ab-initio* data, Int. J. Solids Struct. **135**, 37 (2018).

[79] R. A. Sauer and L. De Lorenzis, An unbiased computational contact formulation for 3D friction, Int. J. Numer. Meth. Eng. **101**, 251 (2015).

[80] F. Shirazian, R. Ghaffari, M. Hu, and R. A. Sauer, Hyperelastic material modeling of graphene based on density functional calculations, Proc. Appl. Math. Mech. **18**, e201800419 (2018).

[81] R. C. Merkle, A proof about molecular bearings, Nanotechnology **4**, 86 (1993).

[82] C. Reddy, S. Rajendran, and K. Liew, Equilibrium configuration and continuum elastic properties of finite sized graphene, Nanotechnology **17**, 864 (2006).

[83] Q. Lu, M. Arroyo, and R. Huang, Elastic bending modulus of monolayer graphene, J. Phys. D: Appl. Phys. **42**, 102002 (2009).